Bull Earthquake Eng (2014) 12:909–938
DOI 10.1007/s10518-013-9557-x

ORIGINAL RESEARCH PAPER

Prediction of the largest peak nonlinear seismic response of asymmetric buildings under bi-directional excitation using pushover analyses

Kenji Fujii

Received: 14 May 2013 / Accepted: 16 November 2013 / Published online: 30 November 2013
© Springer Science+Business Media Dordrecht 2013

Abstract A simplified procedure is proposed to predict the largest peak seismic response of an asymmetric building to horizontal bi-directional ground motion, acting at an arbitrary angle of incidence. The main characteristics of the proposed procedure is as follows. (1) The properties of two independent equivalent single-degree-of-freedom models are determined according to the principal direction of the first modal response in each nonlinear stage, rather than according to the fixed axis based on the mode shape in the elastic stage; the principal direction of the first modal response in each nonlinear stage is determined based on pushover analysis results. (2) The bi-directional horizontal seismic input is simulated as identical spectra of the two horizontal components, and the contribution of each modal response is directly estimated based on the unidirectional response in the principal direction of each. (3) The drift demand at each frame is determined based on four pushover analyses considering the combination of bi-directional excitations. In the numerical example, nonlinear time-history analyses of six four-story torsionally stiff (TS) asymmetric buildings are carried out considering various directions of seismic inputs, and these results are compared with the predicted results. The results show that the proposed procedure satisfactorily predicts the largest peak response displacement at the flexible-side frame of a TS asymmetric building.

Keywords Asymmetric building · Bi-directional excitation · Direction of incidence of seismic input · Equivalent linearization technique · Nonlinear static procedure · Torsional index

1 Introduction

Asymmetric buildings are known to be vulnerable to earthquakes. This is because excessive deformation may occur at the frame of the flexible and/or weaker side owing to unfavorable

K. Fujii (✉)
Department of Architecture and Civil Engineering, Chiba Institute of Technology,
2-17-1 Tsudanuma, Narashino, Chiba 275-0016, Japan
e-mail: kenji.fujii@it-chiba.ac.jp

torsional effects. This may lead to premature failure of the brittle members of the structure and final collapse of the whole building.

In designing of new buildings for earthquake resistance or when conducting seismic evaluations of existing buildings, horizontal ground motion is applied to each of the main orthogonal axes of the building. However, for seismic assessment of asymmetric buildings this procedure may be inadequate because the most critical direction of incidence of the seismic input, which would produce the largest response, may be different from the direction of the building's main orthogonal axes, and the major component of ground motion may act in any direction. The influence of the direction of incidence of the seismic input on the response of the building's structure has been investigated analytically (González 1992; López and Torres 1997; Sudo et al. 1996; Kostinakis et al. 2013) and experimentally (Fujii and Ikeda 2012). The results point to a critical direction of seismic input that produces the largest response.

Therefore, it is essential to carry out 3-dimensional analysis considering all the possible directions of seismic input. However, evaluating the seismic response of a building under all possible seismic intensities using nonlinear dynamic (time-history) analysis is very time-consuming.

Simplified nonlinear analysis procedures, which combine the nonlinear static (pushover) analysis of a multi-degree-of-freedom (MDOF) model, and the response spectrum analysis of an equivalent single-degree-of-freedom (SDOF) model (Saiidi and Sozen 1981; Fajfar and Fischinger 1988), have been widely implemented in seismic design codes and seismic evaluation schemes (ATC-40 1996; FEMA 1997; ASCE 2007; CEN 2004). These procedures work well on the condition that the building oscillates predominantly with a single mode. In recent decades, several researchers have tried to extend these simplified procedures to improve the seismic performance estimates of buildings with plan and/or elevation irregularities (Moghadam and Tso 1996). A review of the research on the seismic behavior of irregular building structures over the last decade can be found in Stefano and Pintucchi (2008).

From the author's point of view, there are three possible approaches when considering the torsional effect for predicting the peak response of asymmetric buildings. The first approach is a combination of nonlinear pushover analyses and linear elastic analyses proposed by Fajfar et al. (Perus and Fajfar 2005; Fajfar et al. 2005). The second approach is a combination of nonlinear pushover analysis representing several mode responses with the application of square-root-of-sum-of-square (SRSS) or complete quadratic combination (CQC) rules in linear elastic analyses, and was proposed by Chopra and Goel (2002, 2004). The third approach combines several pushover analyses and envelopes the results, as proposed by Bosco et al. (2012).

The first approach, named the *Extended N2 method*, is the extended version of the simplified procedure by Fajfar and Fischinger (1988). In this procedure, the peak response of each frame is estimated using the pushover analysis results multiplied by a "correction factor", which is defined using linear elastic analysis. This procedure was verified by Bhatt and Bento (2011), who analyzed three multi-story reinforced concrete (RC) asymmetric buildings with regular elevation, and by D'Ambrisi et al. (2009), who applied the extended N2 method to existing multi-story RC buildings with plan and elevation irregularities. In recent years, the extended N2 method was modified by Kreslin and Fajfar (2010, 2012) by considering the elastic response displacement distribution in both plan and elevation.

The extended N2 method is based on the assumption the elastic envelope of lateral displacements is conservative with respect to the inelastic envelope, as noted by Stefano and Pintucchi (2010). They pointed out that this assumption may be invalid for structures characterized by very high torsional stiffness. Isakovic and Fischinger (2011) performed shaking

table tests on an RC bridge structure and showed that the extended N2 method failed to estimate the peak responses under high seismic intensity because it did not take into account the change in the fundamental mode.

The second approach, called *modal pushover analysis* (MPA), was proposed by Chopra and Goel (2002) for regular buildings considering the higher-mode effect, and was extended for asymmetric buildings (Chopra and Goel 2004). In this approach, the seismic response is estimated using pushover analysis of a MDOF model with a force distribution based on each elastic mode shape, and a spectrum analysis response of independent equivalent SDOF models, and the combination rules, which are applied in linear analysis (the SRSS or CQC rule).

The applicability of the first and second approaches depends strongly on whether the change in the mode shape in the inelastic range is significant. Because the mode shape of an asymmetric building may change significantly, the predicted results based on an elastic mode shape may provide erroneous results.

The third approach, which was proposed by Bosco et al. (2012), estimates the peak response at the stiff and flexible-side frames by enveloping two pushover analyses results. In their procedure, "corrective eccentricity" is the key parameter in the pushover analyses. This may be a promising approach, because the various possible collapse mechanisms resulting from the combination of several mode responses can be properly predicted using a combination of different force distributions. However, because the corrective eccentricity is formulated using the parameters of a single-story building model, and the reliability of its formulation relies strongly on the results of a large number of numerical examples of single-story asymmetric building models, this method may be difficult to apply to more general cases such as multi-story buildings with dual-systems (moment-resisting frame + structural walls) or various dampers, or multi-story buildings with setbacks.

The author has tried to extend the nonlinear static procedure to asymmetric buildings subjected to bi-directional excitation (Fujii et al. 2006; Fujii 2007, 2010, 2011, 2012). A single-story asymmetric building model with elasto-plastic dampers (Fujii et al. 2006) and multi-story asymmetric frame building models (Fujii 2007, 2011) were used and the critical direction of each asymmetric building was determined from the first mode shape and was named *the principal direction of the first modal response*. In these studies, the principal axis of the first modal response was assumed to be fixed in the elastic range. Therefore, its prediction may include a significant error if the shape of the first mode changes significantly.

In 2010, the author proposed a simplified seismic assessment procedure for asymmetric frame buildings considering the critical direction of the seismic input at each nonlinear stage (Fujii 2010). In this procedure, the critical direction of the seismic input, which produces the maximum response at a flexible side frame, was assumed to coincide with the principal direction of the first modal response which was evaluated using pushover analyses results at each nonlinear stage. However, only one-component horizontal ground motion was considered in this procedure; to improve the estimates of this method, bi-directional horizontal ground motion needs to be considered.

In this article, a simplified procedure is proposed to predict the largest peak seismic response of asymmetric buildings, caused by horizontal bi-directional ground motion acting at an arbitrary angle of incidence. This procedure is the extended version of the procedure proposed in Fujii (2010) which accounts only for uni-directional excitation. Note that the procedure presented here is modified from the procedure proposed previously by the author (Fujii 2012) to improve the accuracy at the flexible-side frame in the stronger direction of the building.

In the numerical example, nonlinear time-history analyses of six four-story reinforced concrete asymmetric frame buildings under various directions of seismic input were carried

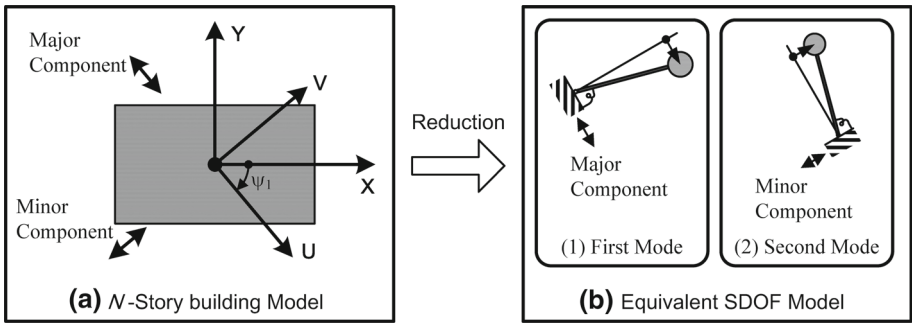

Fig. 1 Concept of the proposed procedure

out and compared with the predicted results. Note that the following discussion focuses only on torsionally stiff (TS) buildings, as in the previous study by the author (Fujii 2010, 2012). The applicability of this procedure for torsionally flexible (TF) buildings is discussed elsewhere.

2 Description of the proposed procedure

2.1 Concept of the proposed procedure

The concept of the proposed procedure is shown in Fig. 1. A set of orthogonal axes U–V in the X–Y plane is considered, with the U-axis being the principal axis of the first modal response (Fujii 2010, 2011). The asymmetric buildings are N-story buildings, with $3N$ degrees of freedom ($3N$-DOFs) oriented for the multi-story model presented here.

The spectra of the two horizontal ground motion components are assumed to be identical; the spectrum of the horizontal minor component is assumed to be the same as that of the major component. López et al. (2006) showed that the ratio of the spectra for the horizontal minor and major components varied between 0.63 and 0.81. Therefore, the identical-component assumption would be expected to provide conservative prediction results. This approach was discussed by López and Torres (1997) for elastic spectrum analysis; here it is applied to estimate the largest peak response using a simplified nonlinear procedure.

The largest peak responses of the first and second modes are obtained independently from the equivalent SDOF models. The prediction of the largest peak response at each frame is based on a set of pushover analyses considering the combination of the two modal responses.

2.2 Outline of proposed procedure

The proposed procedure consists of the following steps:

STEP 1: Pushover analysis of the asymmetric building model (first mode)
STEP 2: Prediction of the peak seismic response of the equivalent SDOF model (first mode)
STEP 3: Pushover analysis of the asymmetric building model (second mode)
STEP 4: Prediction of the peak seismic response of the equivalent SDOF model (second mode)
STEP 5: Prediction of the largest peak response at each frame

The formulations of the equivalent SDOF model can be found in “Appendix 1”.

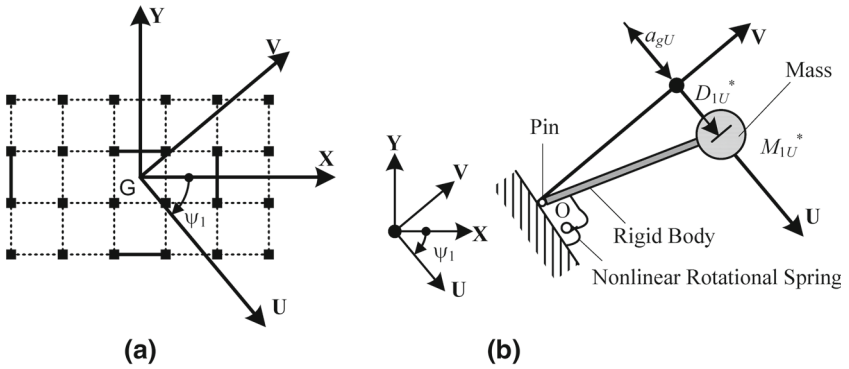

Fig. 2 Equivalent SDOF model (first mode). **a** Plan of asymmetric building structure. **b** Equivalent SDOF model (first mode)

2.2.1 Step 1: Pushover analysis of the asymmetric building model (first mode)

The equivalent SDOF model for the first modal response is shown in Fig. 2. As in Fig. 1, the U-axis of the orthogonal U–V axes indicates the principal axis of the first modal response in the X–Y plane.

The nonlinear properties of the equivalent SDOF model, the equivalent acceleration A^*_{1U} and equivalent displacement D^*_{1U} relationship, referred to as the capacity curve, are determined using the pushover analysis considering the change in shape of the first mode at each nonlinear stage. In this article, the displacement-based mode-adaptive pushover analysis (Fujii 2010) is applied (details of the analysis can be found in "Appendix 2").

The equivalent displacement and acceleration at each loading step n, ${}_nD^*_{1U}$ and ${}_nA^*_{1U}$, are determined from Eqs. (1) and (2), respectively, assuming that the displacement vector at each loading stage $\mathbf{{}_nd}$ is proportional to the first mode vector at each loading stage ${}_n\Gamma_{1U}\mathbf{{}_n\varphi_1}$.

$$ {}_nD^*_{1U} = \frac{{}_n\Gamma_{1U}\mathbf{{}_n\varphi_1^T M_n d}}{{}_nM^*_{1U}} = \frac{\sum_j \left(m_{jn}x_j^2 + m_{jn}y_j^2 + I_{jn}\theta_j^2\right)}{\sqrt{\left(\sum_j m_{jn}x_j\right)^2 + \left(\sum_j m_{jn}y_j\right)^2}}, \tag{1} $$

$$ {}_nA^*_{1U} = \frac{{}_n\Gamma_{1U}\mathbf{{}_n\varphi_1^T {}_nf}_R}{{}_nM^*_{1U}} = \frac{\sum_j \left({}_nf_{RXjn}x_j + {}_nf_{RYjn}y_j + {}_nf_{MZjn}\theta_j\right)}{\sqrt{\left(\sum_j m_{jn}x_j\right)^2 + \left(\sum_j m_{jn}y_j\right)^2}}, \tag{2} $$

where

$$ {}_nM^*_{1U} = {}_n\Gamma^2_{1U}\mathbf{{}_n\varphi_1^T M_n \varphi_1} = \frac{\left(\sum_j m_{jn}x_j\right)^2 + \left(\sum_j m_{jn}y_j\right)^2}{\sum_j m_{jn}x_j^2 + \sum_j m_{jn}y_j^2 + \sum_j I_{jn}\theta_j^2}, \tag{3} $$

$$ {}_n\Gamma_{1U} = \frac{\mathbf{{}_n\varphi_1^T M_n \alpha_U}}{\mathbf{{}_n\varphi_1^T M_n \varphi_1}} = \frac{\sqrt{\left(\sum_j m_{jn}x_j\right)^2 + \left(\sum_j m_{jn}y_j\right)^2}}{\sum_j m_{jn}x_j^2 + \sum_j m_{jn}y_j^2 + \sum_j I_{jn}\theta_j^2}, \tag{4} $$

$$\mathbf{M} = \begin{bmatrix} \mathbf{M_0} & \mathbf{0} & \mathbf{0} \\ \mathbf{0} & \mathbf{M_0} & \mathbf{0} \\ \mathbf{0} & \mathbf{0} & \mathbf{I_0} \end{bmatrix}, \quad \mathbf{M_0} = \begin{bmatrix} m_1 & & 0 \\ & \ddots & \\ 0 & & m_N \end{bmatrix}, \quad \mathbf{I_0} = \begin{bmatrix} I_1 & & 0 \\ & \ddots & \\ 0 & & I_N \end{bmatrix}, \tag{5}$$

$$_{n}\mathbf{d} = \{{}_{n}x_1 \ \cdots \ {}_{n}x_N \ {}_{n}y_1 \ \cdots \ {}_{n}y_N \ {}_{n}\theta_1 \ \cdots \ {}_{n}\theta_N\}^{\mathbf{T}}, \tag{6}$$

$$_{n}\mathbf{f_R} = \{{}_{n}f_{RX1} \ \cdots \ {}_{n}f_{RXN} \ {}_{n}f_{RY1} \ \cdots \ {}_{n}f_{RYN} \ {}_{n}f_{MZ1} \ \cdots \ {}_{n}f_{MZN}\}^{\mathbf{T}}, \tag{7}$$

$$_{n}\boldsymbol{\varphi_1} = \{{}_{n}\phi_{X11} \ \cdots \ {}_{n}\phi_{XN1} \ {}_{n}\phi_{Y11} \ \cdots \ {}_{n}\phi_{YN1} \ {}_{n}\phi_{\Theta 11} \ \cdots \ {}_{n}\phi_{\Theta N1}\}^{\mathbf{T}}, \tag{8}$$

$$_{n}\boldsymbol{\alpha_U} = \{\cos{}_{n}\psi_1 \ \cdots \ \cos{}_{n}\psi_1 \ -\sin{}_{n}\psi_1 \ \cdots \ -\sin{}_{n}\psi_1 \ 0 \ \cdots \ 0\}^{\mathbf{T}}, \tag{9}$$

$$\cos{}_{n}\psi_1 = \frac{\sum_j m_{jn}\phi_{Xj1}}{\sqrt{\left(\sum_j m_{jn}\phi_{Xj1}\right)^2 + \left(\sum_j m_{jn}\phi_{Yj1}\right)^2}} = \frac{\sum_j m_{jn}x_j}{\sqrt{\left(\sum_j m_{jn}x_j\right)^2 + \left(\sum_j m_{jn}y_j\right)^2}}, \tag{10}$$

$$\sin{}_{n}\psi_1 = \frac{-\sum_j m_{jn}\phi_{Yj1}}{\sqrt{\left(\sum_j m_{jn}\phi_{Xj1}\right)^2 + \left(\sum_j m_{jn}\phi_{Yj1}\right)^2}} = \frac{-\sum_j m_{jn}y_j}{\sqrt{\left(\sum_j m_{jn}x_j\right)^2 + \left(\sum_j m_{jn}y_j\right)^2}}. \tag{11}$$

In Eqs. (1)–(11), m_j and I_j are the mass and moment of inertia of the jth floor, respectively, ${}_{n}M^*_{1U}$ is the equivalent first modal mass with respect to the U-axis at each nonlinear stage, and ${}_{n}\psi_1$ is the angle of incidence of the principal axis (the U-axis) at each nonlinear stage. Note that the reference axis considering the first mode response (U-axis) is displacement-dependent; it changes at each nonlinear stage as the first mode vector changes.

2.2.2 *Step 2: Prediction of the peak seismic response of the equivalent SDOF model (first mode)*

The largest peak equivalent displacement $D^*_{1U\ \max}$ and equivalent acceleration $A^*_{1U\ \max}$ are obtained using the equivalent linearization technique (Otani 2000). Alternatively, the inelastic response spectrum may be used to obtain the seismic demand curve of the equivalent SDOF model.

2.2.3 *Step 3: Pushover analysis of the asymmetric building model (second mode)*

From the results of Steps 1 and 2, the first mode vector corresponding to $D^*_{1U\ \max}$, $\Gamma_{1Uie}\boldsymbol{\varphi_{1ie}}$, is obtained. The second mode vector, $\Gamma_{2Vie}\boldsymbol{\varphi_{2ie}}$, is then determined from Eq. (12), in terms of $\Gamma_{1Uie}\boldsymbol{\varphi_{1ie}}$ and the second mode vector in the elastic range $\Gamma_{2Ve}\boldsymbol{\varphi_{2e}}$, considering the orthogonal condition of the mode vector.

$$\Gamma_{2Vie} = \frac{\boldsymbol{\varphi}^{\mathbf{T}}_{\mathbf{2ie}}\mathbf{M}\boldsymbol{\alpha}_{\mathbf{Vie}}}{\boldsymbol{\varphi}^{\mathbf{T}}_{\mathbf{2ie}}\mathbf{M}\boldsymbol{\varphi}_{\mathbf{2ie}}}, \quad \boldsymbol{\varphi}_{\mathbf{2ie}} = \boldsymbol{\varphi}_{\mathbf{2e}} - \frac{\boldsymbol{\varphi}^{\mathbf{T}}_{\mathbf{2e}}\mathbf{M}\boldsymbol{\varphi}_{\mathbf{1ie}}}{\boldsymbol{\varphi}^{\mathbf{T}}_{\mathbf{1ie}}\mathbf{M}\boldsymbol{\varphi}_{\mathbf{1ie}}}\boldsymbol{\varphi}_{\mathbf{1ie}}, \tag{12}$$

where

$$\boldsymbol{\alpha}_{\mathbf{Vie}} = \{\sin\psi_{1ie} \ \cdots \ \sin\psi_{1ie} \ \cos\psi_{1ie} \ \cdots \ \cos\psi_{1ie} \ 0 \ \cdots \ 0\}^{\mathbf{T}}, \tag{13}$$

$$\cos\psi_{1ie} = \frac{\sum_j m_j \phi_{Xj1ie}}{\sqrt{\left(\sum_j m_j \phi_{Xj1ie}\right)^2 + \left(\sum_j m_j \phi_{Yj1ie}\right)^2}}, \tag{14}$$

$$\sin\psi_{1ie} = -\frac{\sum_j m_j \phi_{Yj1ie}}{\sqrt{\left(\sum_j m_j \phi_{Xj1ie}\right)^2 + \left(\sum_j m_j \phi_{Yj1ie}\right)^2}}. \tag{15}$$

Next, another pushover analysis of an MDOF model is carried out to obtain the force–displacement relationship representing the second mode response by applying the invariant force distribution $\mathbf{P}_2$ determined by Eq. (16).

$$\mathbf{P_2} = \mathbf{M}\left(\Gamma_{2Vie}\boldsymbol{\varphi}_{\mathbf{2ie}}\right). \tag{16}$$

The equivalent displacement ${}_nD^*_{2V}$ and acceleration ${}_nA^*_{2V}$ of the equivalent SDOF model representing the second modal response at each loading step n are determined by Eq. (17).

$${}_nD^*_{2V} = \frac{\Gamma_{T2Vie}\boldsymbol{\varphi}^{\mathbf{T}}_{\mathbf{T2ie}}\mathbf{M_n d}}{M^*_{2Vie}}, \quad {}_nA^*_{2V} = \frac{\Gamma_{T2Vie}\boldsymbol{\varphi}^{\mathbf{T}}_{\mathbf{2ie}}\mathbf{n}\mathbf{f_R}}{M^*_{2Vie}}, \tag{17}$$

$$M^*_{2Vie} = \Gamma^2_{2Vie}\boldsymbol{\varphi}^{\mathbf{T}}_{\mathbf{2ie}}\mathbf{M}\boldsymbol{\varphi}_{\mathbf{2ie}}. \tag{18}$$

In Eq. (18), M^*_{2Vie} is the equivalent second modal mass with respect to the V-axis determined in terms of $\Gamma_{2Vie}\boldsymbol{\varphi}_{\mathbf{2ie}}$.

2.2.4 Step 4: Prediction of the peak seismic response of the equivalent SDOF model (second mode)

The largest peak equivalent displacement $D^*_{2V\ \max}$ and the equivalent acceleration $A^*_{2V\ \max}$ for the second modal response are obtained using the equivalent linearization technique as discussed in Step 2. Note that the spectrum used in Step 2 is used again for the prediction of the second mode response.

2.2.5 Step 5: Prediction of the largest peak seismic response at each frame

The scheme for predicting the largest peak seismic response at each frame is shown in Fig. 3. The four force distributions are determined as the sum of the contribution of the first and second modal responses. The largest peak seismic response is then predicted as the envelope of the four pushover analyses results. Details of the largest peak response prediction at each frame are described below:

1. Determine the four combined forces $\mathbf{P}^+_{\mathbf{U}}$, $\mathbf{P}^-_{\mathbf{U}}$, $\mathbf{P}^+_{\mathbf{V}}$, and $\mathbf{P}^-_{\mathbf{V}}$ from Eq. (19).

$$\begin{cases} \mathbf{P}^{\pm}_{\mathbf{U}} = \mathbf{M}\left(\Gamma_{1Uie}\boldsymbol{\varphi}_{\mathbf{1ie}}A^*_{1U\ \max} \pm 0.5\Gamma_{T2Vie}\boldsymbol{\varphi}_{\mathbf{2ie}}A^*_{2V\ \max}\right) \\ \mathbf{P}^{\pm}_{\mathbf{V}} = \mathbf{M}\left(\pm 0.5\Gamma_{1Uie}\boldsymbol{\varphi}_{\mathbf{T1ie}}A^*_{1U\ \max} + \Gamma_{2Vie}\boldsymbol{\varphi}_{\mathbf{2ie}}A^*_{2V\ \max}\right) \end{cases}. \tag{19}$$

2. Perform pushover analyses using $\mathbf{P}^+_{\mathbf{U}}$ and $\mathbf{P}^-_{\mathbf{U}}$ until the equivalent displacement ${}_nD^*_{\mathbf{U}}$ calculated by Eq. (20) reaches $D^*_{1U\ \max}$ obtained from Step 2 (referred to as Pushover-1U and 2U, respectively); similarly, $\mathbf{P}^+_{\mathbf{V}}$ and $\mathbf{P}^-_{\mathbf{V}}$ are used in the analysis until the equivalent displacement ${}_nD^*_V$ calculated using Eq. (20) reaches $D^*_{2V\ \max}$ obtained from Step 4 (referred to as Pushover-1V and 2V, respectively):

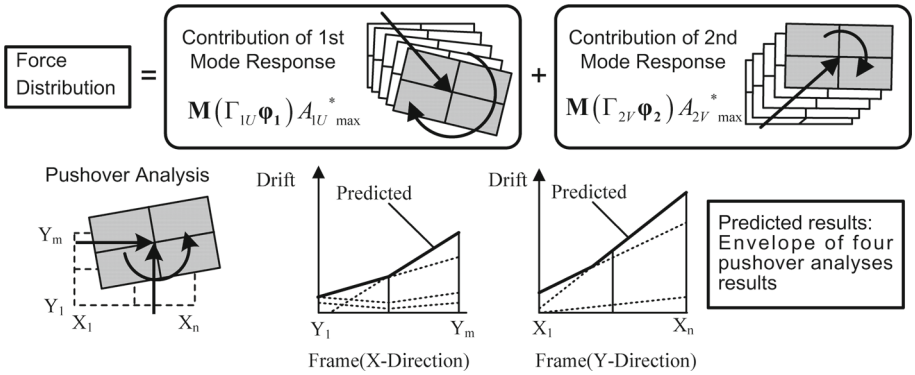

Fig. 3 Prediction scheme for the peak response at each frame using pushover analyses

$$\begin{cases} {}_nD^*_U = \Gamma_{1Uie}\boldsymbol{\varphi}^{\mathbf{T}}_{\mathbf{1ie}}\mathbf{M_n d}/M^*_{1Uie} \\ {}_nD^*_V = \Gamma_{2Vie}\boldsymbol{\varphi}^{\mathbf{T}}_{\mathbf{2ie}}\mathbf{M_n d}/M^*_{2Vie} \end{cases}. \tag{20}$$

In Eq. (20), M^*_{1Uie} is the equivalent first modal mass with respect to the U-axis determined in terms of $\Gamma_{1Uie}\boldsymbol{\varphi}_{\mathbf{1ie}}$.

3. Determine the largest peak response at each frame from the envelope of (a) Pushover-1U and 2U and (b) Pushover-1V and 2V.

Note that Step 5 is different from the previous study (Fujii 2012) in which this procedure used only two pushover analyses (using $\mathbf{P}^+_{\mathbf{U}}$ and $\mathbf{P}^-_{\mathbf{U}}$) to predict the largest peak seismic response at the flexible-edge frame in the weaker direction of the building models. In this article, four pushover analyses are performed to improve the accuracy at the flexible-side frame in the stronger direction.

3 Building and ground motion data

3.1 Building data

In this study, six four-story asymmetric buildings were investigated. Figures 4 and 5 show the plans of the six building models: two with uni-directional eccentricity (Models A1 and A2) and four with bi-directional eccentricity (Models B1, B2, B3, and B4).

The height of the first story is 4.0 m and the upper stories are 3.6 m high. The floor mass m_j and moment of inertia I_j ($j = 1{-}4$) are assumed as 524.9 t and 4.37×10^4 tm^2, respectively. The cross sections of the beams (second floor to the roof) and columns are 350×650 and 600×600 mm, respectively. The thickness of the structural wall is 220 mm. The columns are assumed to be supported as fixed-ends by the foundation. The compressive strength of the concrete, σ_B, is assumed to be 24 N/mm^2. In addition, SD345 steel (yield strength: $\sigma_y = 345$ N/mm^2) is used for the longitudinal reinforcement, and SD295 steel ($\sigma_y = 295$ N/mm^2) is used for the shear reinforcement. Each frame structure is designed according to the weak-beam strong-column concept; the longitudinal reinforcements of the concrete sections are determined so that the potential hinges are located at all the beam-ends and bottoms of the columns and the structural wall in the first story. Sufficient shear reinforcement is assumed to be provided to prevent premature shear failure. Table 1 shows

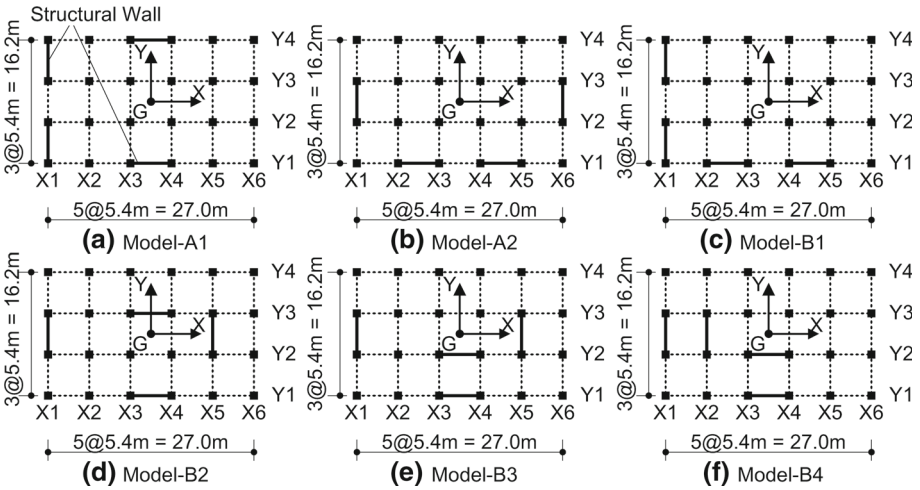

Fig. 4 Plans of the six model buildings

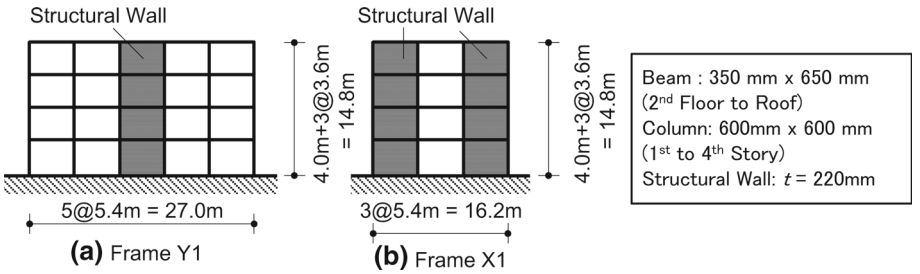

Fig. 5 Elevation of the model buildings (Model-A1)

Table 1 Longitudinal reinforcement of each member

Member	Location	Reinforcement
Boundary beam	2nd to roof floor	6-D25 (top and bottom)
Beam	4nd and roof floor	3-D25 (top and bottom)
	2nd to 3rd floor	4-D25 (top and bottom)
Column	2nd to 4th story	20-D29 (top and bottom)
	1st story	20-D29 (top), 8-D29 (bottom)
Structural wall	All story	D10@200Double

the longitudinal reinforcement of each member. The crack moment M_c and yield moment M_y of each concrete member are calculated according to the AIJ Design Guidelines (AIJ 1999). The base shear coefficients obtained from the planar pushover analysis in both the X- and Y-directions, which are the values when the roof displacement reaches 1 % of the total height H_N, are shown in Table 2.

The building structure is modeled as a pseudo 3-dimensional frame model in which the floor diaphragms are assumed to be rigid in their own planes with no out-of-plane stiffness, and the frames oriented in the X- and Y-directions are modeled independently. One-component

Table 2 Base shear coefficients of building models based on planar frame analysis

Model	X-Dir.	Y-Dir.
Model-A1	0.532	0.455
Model-A2	0.522	0.510
Model-B1	0.522	0.455
Model-B2	0.546	0.525
Model-B3	0.546	0.525
Model-B4	0.546	0.525

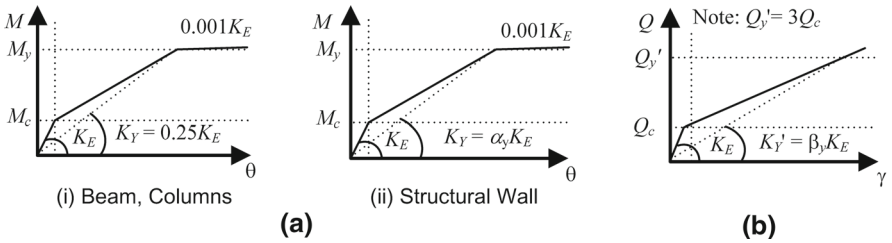

Fig. 6 Envelope of the force-deformation relationship of nonlinear springs. **a** M–θ relationship (flexural spring). **b** Q–γ relationship (shear spring of stuctural wall)

model, with two nonlinear flexural springs at both ends and one nonlinear shear spring in the middle of the line element, is used for all the concrete beams, columns, and structural walls. At the end of each member, rigid zones are assumed to identify the depth of the intersecting members. To determine the flexibility of the nonlinear flexural springs, an anti-symmetric curvature distribution is assumed for the beams and columns, and a uniform curvature distribution is assumed for the structural walls. Figure 6a, b show the envelope curve for the force-deformation relationship of each nonlinear spring. The envelopes are assumed to be symmetric in both the positive and negative loading directions. As shown in Fig. 6a, the secant stiffness degradation ratio of the flexural spring at the yield point, α_y, is assumed to be 0.25 for all the beams and columns. For the structural walls at the bottom of the first story, α_y is assumed to be 0.12 and for all other points it is 0.19. In Fig. 6b, the secant stiffness degradation ratio of the shear spring at the "yield point" β_y is assumed to be 0.16. The axial stiffness of the columns and walls is assumed to remain elastic, and the effects of the biaxial bending and axial–flexural interaction are ignored. The torsional stiffness of the members is also ignored. No second-order effect (e.g., the P-Δ effect) is considered. The Muto hysteretic model (Muto et al. 1974) with one modification is used to model the flexural springs, as shown in Fig. 7a. Specifically, the unloading stiffness after yielding decreases in proportion to $\mu^{-0.5}$ (μ is the ductility ratio of the flexural spring) to represent the degradation of the unloading stiffness after the yielding of the RC members, as in the model of Otani (1981). The origin-oriented model (Fig. 7b) is used to model the shear spring of the structural wall. The shear springs of the beams and columns are assumed to be elastic. The damping matrix is assumed to be proportional to the instant stiffness matrix with 3 % of the critical damping for the first mode.

Figure 8 shows the natural modes of the building models in the elastic range. Here, T_{ke} is the kth natural period in the elastic range, ψ_{ke} is the angle of incidence of the principal direction of the kth modal response in the elastic range with its tangent given by Eq. (21), and $R_{\rho ke}$ is the torsional index of the kth mode (Fujii and Ikeda 2012) in the elastic range, as defined by Eq. (22).

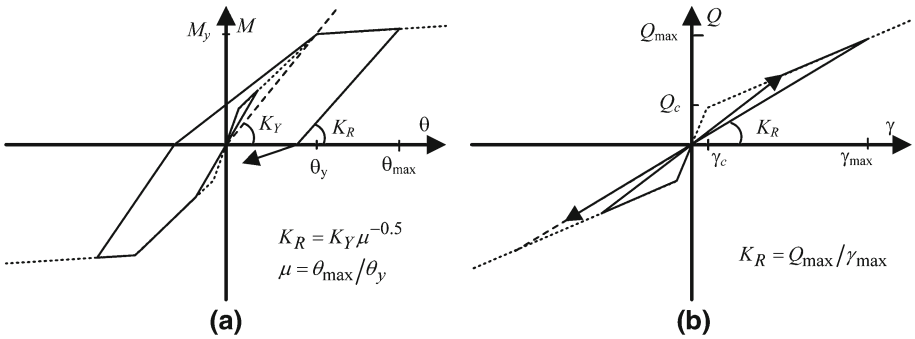

Fig. 7 Hysteretic model for the nonlinear flexure spring and shear spring. **a** Flexural spring (modified Muto model). **b** Shear spring (origin-oriented model)

$$\tan \psi_{ke} = -\sum_j m_j \phi_{Yjke} \Big/ \sum_j m_j \phi_{Xjke}, \tag{21}$$

$$R_{\rho ke} = \sqrt{\sum_j I_j \phi^2_{\Theta jke} \Big/ \left(\sum_j m_j \phi^2_{Xjke} + \sum_j m_j \phi^2_{Yjke} \right)}. \tag{22}$$

The formulation of $R_{\rho ke}$ is summarized in "Appendix 3".

As shown in Fig. 8, the principal direction of the first three modes coincides with the main orthogonal axes of the building models (the X- and Y-axes) for the building models with uni-directional eccentricity (Models A1 and A2); however, for the building models with bi-directional eccentricity (Models B1–B4) the principal direction of the first three modes is not along the X- and Y-axes. In all the building models, the first mode is predominantly translational ($R_{\rho 1e} < 1$) and the second mode is almost purely translational ($R_{\rho 2e} \ll 1$) while the third mode is predominantly torsional ($R_{\rho 3e} > 1$) and the angles between the principal directions of the first two modes are close to 90° (within 89.6°–90.4°). Because the first and second modes are predominantly translational ($R_{\rho 1e},\ R_{\rho 2e} < 1$) in all the building models, they are classified as TS systems in this article. Further discussion can be found in "Appendix 4".

3.2 Ground motion data

In this study, the seismic excitation was considered to be bi-directional in the X–Y plane, and three sets of artificial ground motions were generated.

The target elastic spectrum of the "major" components with 5 % critical damping $S_{A1}(T, 0.05)$, determined from the Building Standard Law of Japan (BCJ 2010) considering soil conditions, is calculated using Eq. (23), where T represents the natural periods of the SDOF model.

$$S_{A1}(T, 0.05) = \begin{cases} 4.8 + 45T \text{ m/s}^2 & : T < 0.16 \text{ s} \\ 12.0 & : 0.16 \text{ s} \le T < 0.576 \text{ s} \\ 12.0(0.576/T) & : T \ge 0.576 \text{ s} \end{cases}. \tag{23}$$

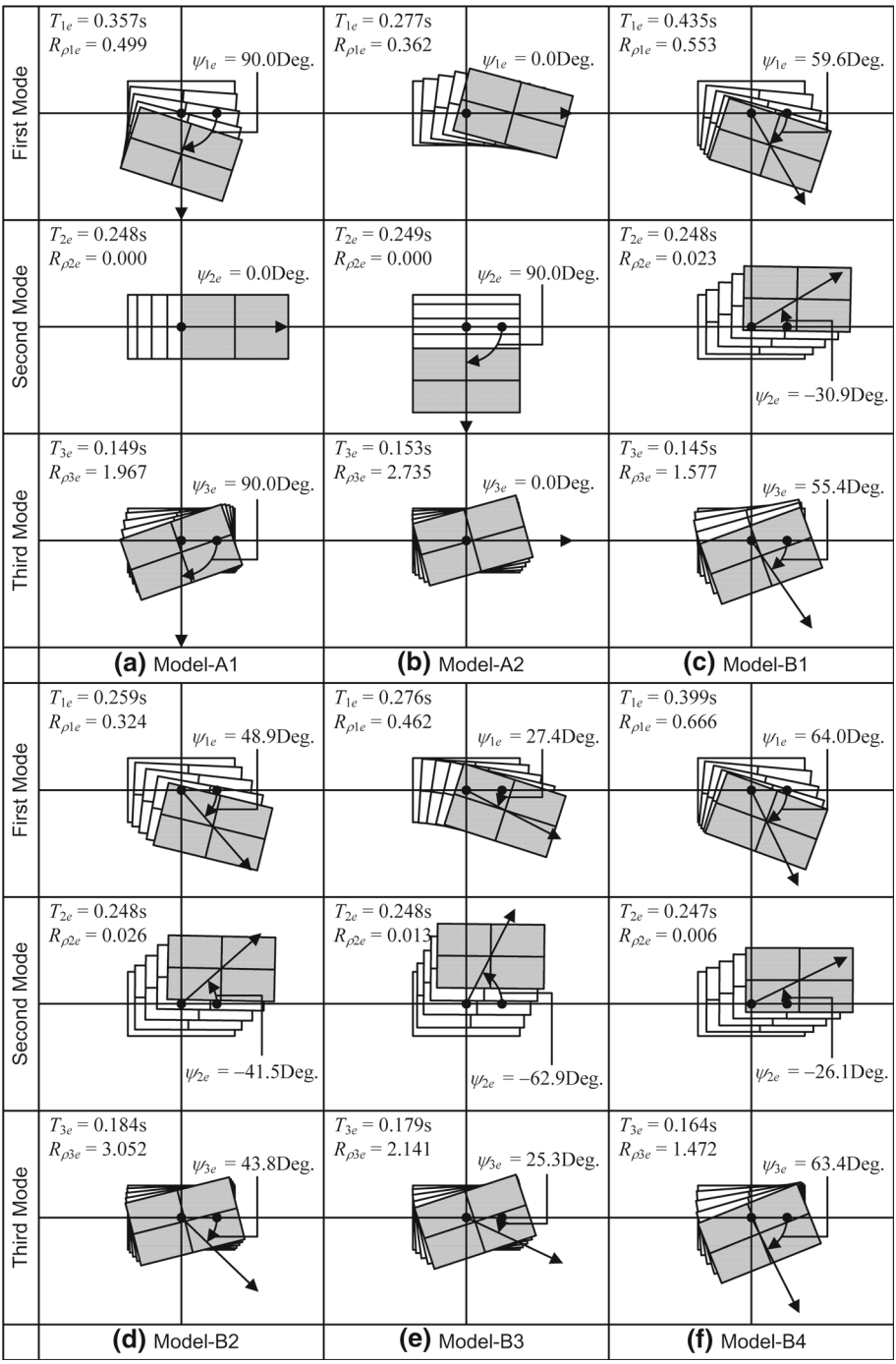

Fig. 8 Shape of the first three natural modes of the building models in the elastic range

The target spectrum of the "minor" components $S_{A2}(T, 0.05)$ is reduced by the parameter γ. Here, the parameter γ is set to 0, 0.5, 0.7, and 1.0; for $\gamma = 0$ the ground motion is considered unidirectional whereas when $\gamma = 1.0$ the spectra of the two horizontal components are identical, as is assumed for the prediction of the largest peak response.

The phase angles are given by uniform random values and the Jennings type envelope function $e(t)$ proposed by the Building Center of Japan, as shown in Eq. (24).

$$e(t) = \begin{cases} (t/5)^2 & : 0\,\mathrm{s} \le t < 5\,\mathrm{s} \\ 1 & : 5\,\mathrm{s} \le t < 35\,\mathrm{s} \\ \exp\{-0.027(t-35)\} & : 35\,\mathrm{s} \le t < 120\,\mathrm{s} \end{cases} . \tag{24}$$

The elastic acceleration response spectra of the artificial ground motion with 5 % critical damping are shown in Fig. 9, and the artificial ground motions are listed in Table 3. The artificial ground motions used in this paper are generated independently, i.e., there is no correlation between the sets of two components. As shown in the table, the correlation coefficients of all three sets are close to zero although the envelope functions of the two components are the same; therefore, the two horizontal components can be considered independent of each other.

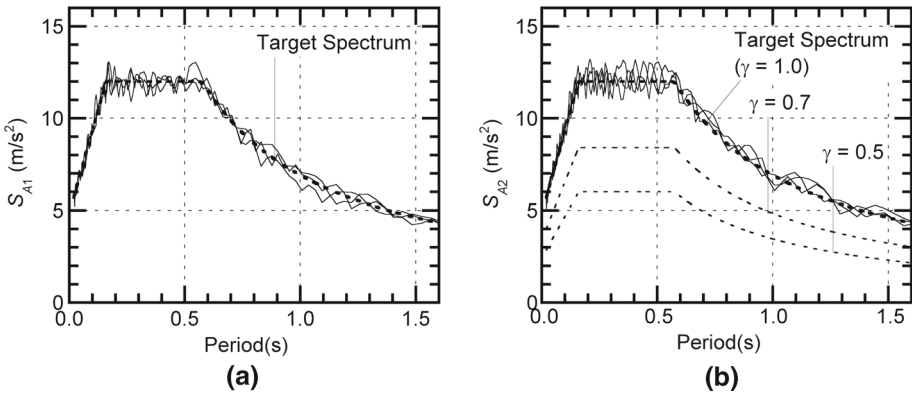

Fig. 9 Elastic acceleration response spectra for simulated ground motion. **a** Major component. **b** Minor component

Table 3 List of artificial ground motions

Ground motion ID	Max. acc. (m/s^2)					Correlation coefficient
	"Major"	"Minor"[a]				
		$\gamma = 0.0$	$\gamma = 0.5$	$\gamma = 0.7$	$\gamma = 1.0$	
Art-001	5.152	0.000	2.200	3.080	4.400	0.0047
Art-002	5.174	0.000	2.344	3.282	4.688	−0.0313
Art-003	5.189	0.000	2.257	3.160	4.514	0.0445

[a] The acceleration of the "Minor" component is reduced by multiplying the artificial motion generated as the "Minor" component ($\gamma = 1.0$) by γ

4 Validation of the proposed procedure

4.1 Pushover analyses results and prediction of the peak response of the equivalent SDOF model

For the prediction of the largest peak response of the equivalent SDOF model representing both the first and second mode, the same elastic response spectrum defined by Eq. (23), is used.

Figure 10 shows the prediction curves of the largest peak response of the equivalent SDOF model obtained in Steps 2 and 4 of the proposed procedure, for all six models. The intersection point of the capacity and demand curves represents the predicted peak response of the equivalent SDOF model.

To investigate the change in critical direction in the inelastic range, the relationship between ${}_n\psi_1$ and ${}_nD^*_{1U}$ is investigated based on the pushover analysis results in Step 1, where ${}_n\psi_1$ is the angle of incidence of the principal axis of the first modal response (the U-axis) with respect to the X-axis in each loading stage, and ${}_nD^*_{1U}$ is the corresponding equivalent displacement. Figure 11 shows the relationship between ${}_n\psi_1$ and ${}_nD^*_{1U}$ for all six models. The angle of incidence of the U-axis with respect to the X-axis in the elastic range, ψ_{1e}, is also shown. The black dot "•" on the ${}_n\psi_1 - {}_nD^*_{1U}$ curve corresponds to the point of the predicted peak equivalent displacement of the first modal response, $D^*_{1U\ \max}$.

Figure 11a, b show the curves for the building models with uni-directional eccentricity (Models A1 and A2) where ${}_n\psi_1$ remains unchanged. In contrast, Fig. 11c–f indicate that significant changes to ${}_n\psi_1$ may occur in the building models with bi-directional eccentricity (Models B1–B4); the change of ${}_n\psi_1$ is negligible in Model B1 (Fig. 11c) and relatively small (about 10°) in Model B4 (Fig. 11f), while the difference between ${}_n\psi_1$ and ψ_{1e} is significant (close to 40°) for Models B2 and B3 (Fig. 11d, e).

4.2 Comparison of the predicted results with the results of the time-history analyses

The validity of the proposed procedure is evaluated as follows. In the first part (Case 1), the predicted peak responses are compared with the results of the nonlinear time-history analyses under bi-directional excitations in which the spectra of the two horizontal components are identical ($\gamma = 1.0$). In the second part (Case 2), nonlinear time-history analyses are carried out for various values of γ, the spectral ratio of "minor" to "major" components, ($\gamma = 0$, 0.5, and 0.7) and various directions of incidence of seismic input. Finally, the largest peak responses for each value of γ are compared with the predicted results. Note that in both Cases 1 and 2, ψ, the angle of incidence of the "major" component with respect to the X-axis, varies at 15°-intervals from $(\psi_1 - 90)°$ to $(\psi_1 + 90)°$, where ψ_1 is the angle of incidence of the U-axis corresponding to the predicted peak equivalent displacement of the first modal response $D^*_{1U\ \max}$ shown in Fig. 11. Therefore, $3 \times 13 = 39$ cases were considered for the nonlinear time-history analysis of each building model in Case 1, while $3 \times 3 \times 13 = 117$ cases were considered in Case 2.

4.2.1 Case 1: peak response subjected to two ground motion components with identical response spectra

Figure 12 shows comparisons of the peak roof displacement at each frame for all six models. The results of four pushover analyses (envelope of $\mathbf{P}^{\pm}_{\mathbf{U}}$ and $\mathbf{P}^{\pm}_{\mathbf{V}}$) from this study and two pushover analyses (envelope of $\mathbf{P}^{\pm}_{\mathbf{U}}$) from a previous study (Fujii 2012), are also shown. The

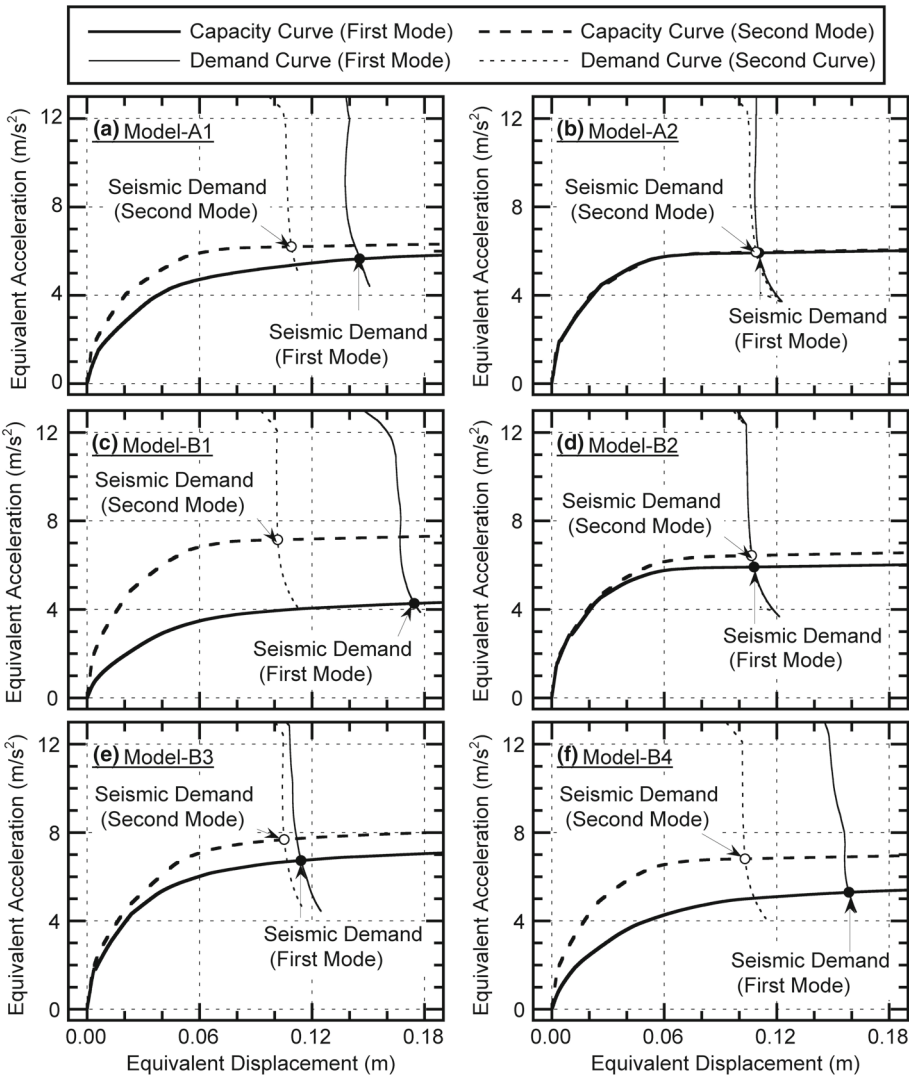

Fig. 10 Prediction of the largest peak response of the equivalent SDOF model using the equivalent linearization technique. The intersection point for the capacity and demand curves indicates the predicted peak response of the equivalent SDOF model

predicted peak response from the envelope of $\mathbf{P}_{\mathbf{U}}^{\pm}$ and $\mathbf{P}_{\mathbf{V}}^{\pm}$ agrees well with the results of the time-history analyses except for a stiff-side edge frame in one direction of some models (frame X1 of Models A1, B1, and B4 and frame Y1 of Model B3). This is because only two (the first and second) modal responses are considered in the proposed procedure to predict the peak response, while the contribution of the third and higher mode response to the peak response may be significant in frames such as frame X1 of Models A1 and B1.

Note that the predicted peak response from the envelope of $\mathbf{P}_{\mathbf{U}}^{\pm}$ underestimates the results of the time-history analyses at all the frames in the X-direction of Models A1, B1, B2, B3,

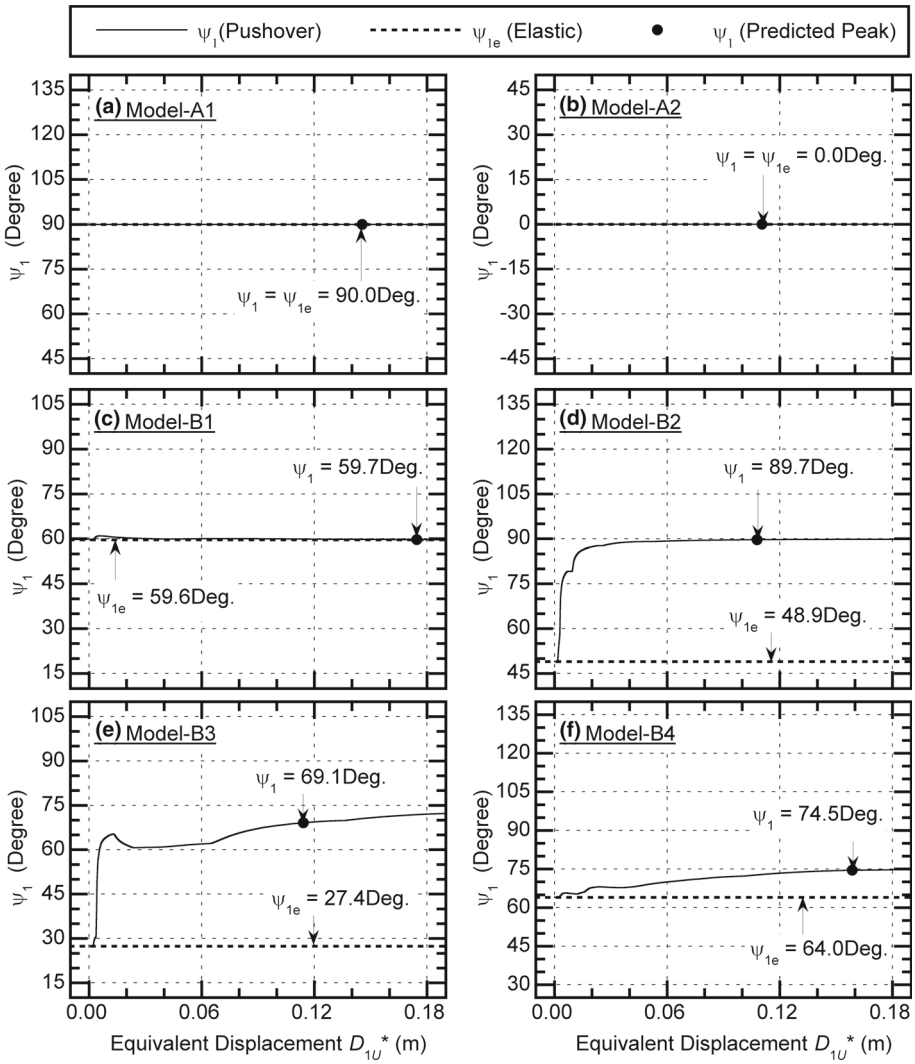

Fig. 11 Change of the angle of incidence for the principal direction of the first modal response with respect to the X-axis

and B4, while it underestimates the results of the time-history analyses at all the frames in the Y-direction of Model A2. As can clearly be seen, using the results of the four pushover analyses is the key to the improvement on the results of the previous study (Fujii 2012). In the following discussion, the predicted peak response from the results of the four pushover analyses (envelope of $\mathbf{P}_{\mathbf{U}}^{\pm}$ and $\mathbf{P}_{\mathbf{V}}^{\pm}$) is considered.

Figures 13 and 14 compare the predicted peak story drift of the stiff-edge frames (frames Y1 and X1) and flexible-edge frames (frames Y4 and X6) with the results of the time-history analyses. The predicted results for the flexible-edge frames are in good agreement with the results of the time-history analyses for all models, while the predicted results may

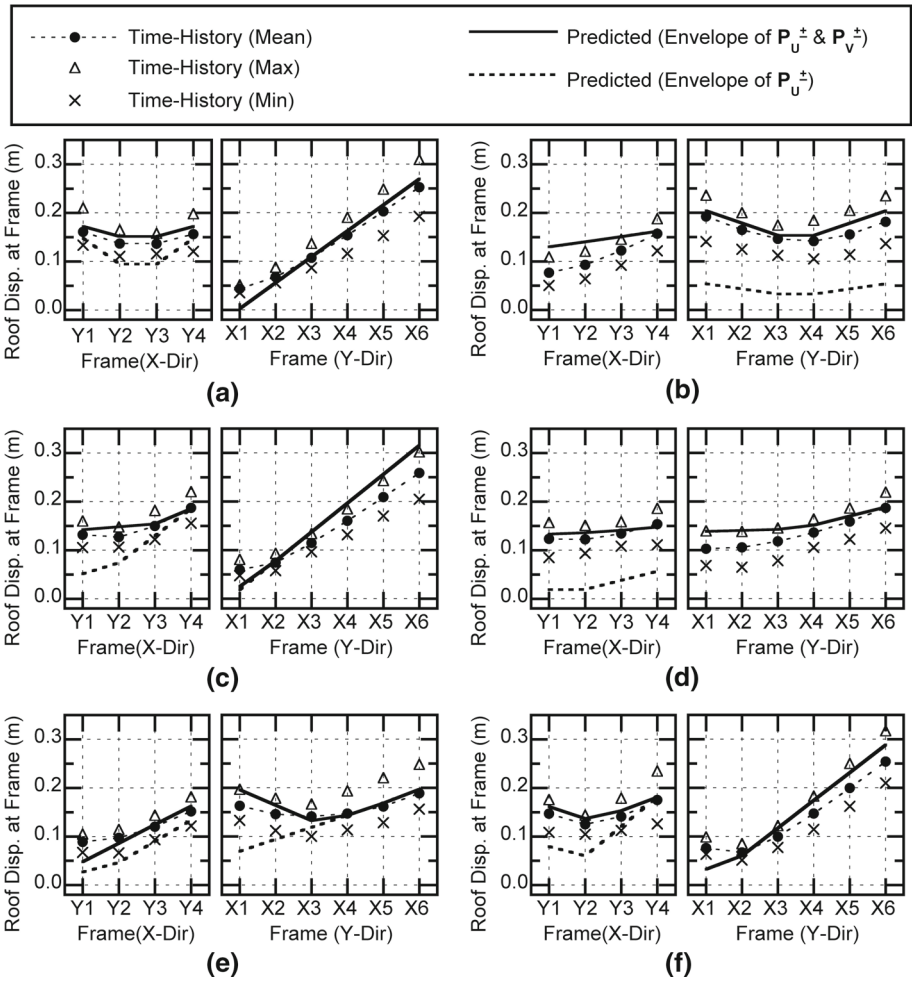

Fig. 12 Comparisons of the peak roof displacement at each frame ($\gamma = 1.0$). **a** Model-A1. **b** Model-A2. **c** Model-B1. **d** Model-B2. **e** Model-B3. **e** Model-B4

be underestimated significantly in one direction for the stiff-edge frames (e.g., frame X1 of Model A1, Fig. 13a).

The results of the analyses of the responses for the six building models suggest that the peak response displacement in the flexible-side frames of asymmetric building models under bi-directional excitation can be satisfactorily predicted by the procedure presented here when the spectra of the two horizontal components are identical. Note that even in the case of Models B2 and B3, where the principal direction of the first modal response changes significantly from that of the elastic stage (Fig. 11d, e), the predicted largest peak responses agree very well with those of the time-history analyses. Therefore, the proposed procedure can be applied to asymmetric buildings where the change in the principal direction of the first modal response is significant; this point is one of the biggest improvements on the procedure previously presented (Fujii et al. 2006; Fujii 2007, 2011).

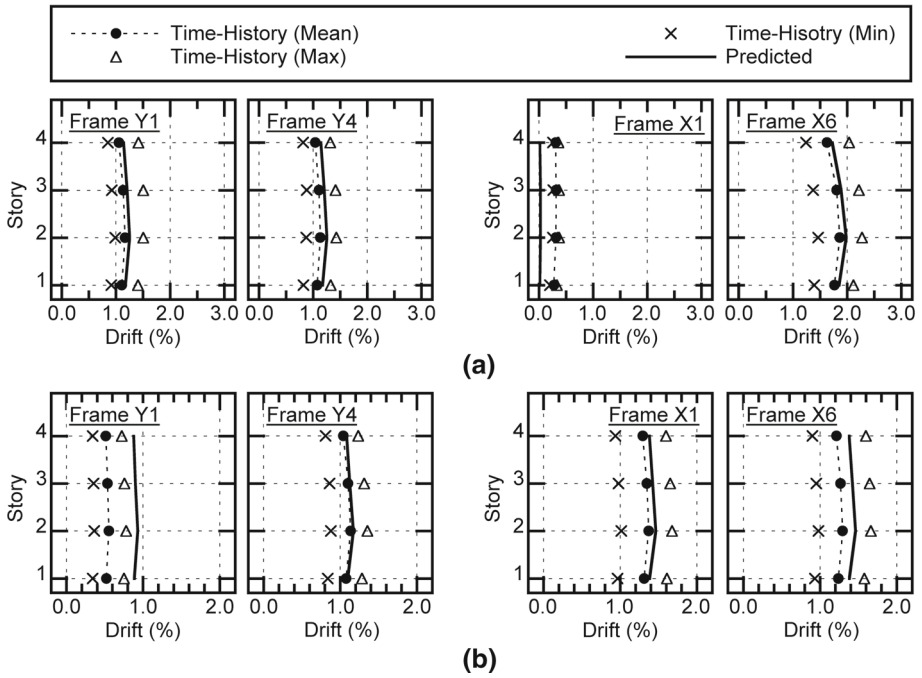

Fig. 13 Comparisons of the peak story drift at each frame (Model A series). **a** Model-A1. **b** Model-A2

4.2.2 Case 2: peak response subjected to two ground motion components with identical spectral shapes and different intensities

In this section, the discussion will focus on the peak response of the flexible-edge frames, because the proposed procedure is extremely accurate for predicting the peak response at the flexible-edge frames for $\gamma = 1.0$ (Case 1).

Figures 15 and 16 show the influence of the direction of incidence of the "major" component on the peak roof displacement at flexible-edge frames. The plot for $\gamma = 0.0, 0.5,$ and 0.7 shows the average of the results of the time-history analyses for three sets of ground motions, while the plot "$\gamma = 1.0$ (Ave.)" indicates the average of 36 cases (three sets of ground motions $\times$ 12 directions). Also shown is the largest peak response predicted by the proposed procedure, and ψ_1, the angle of incidence of the U-axis corresponding to the predicted peak equivalent displacement of the first modal response, $D^*_{1U\ \max}$ shown in Fig. 11.

These figures indicate that, as expected, the plot "$\gamma = 1.0$ (Ave.)" is close to the predicted peak response, and it envelopes almost all the results of $\gamma = 0.0, 0.5,$ and 0.7. This is similar to the results in the elastic response case discussed by López and Torres (1997).

These figures also show that when $\gamma = 0.0, 0.5,$ and 0.7, the largest peak response at the flexible-edge frame in the Y-direction occurs when the angle of incidence of the "major" component ψ is close to ψ_1 for all models except Model A2. This is because, for all the models except Model A2, the contribution of the first modal response is significant for frame X6, while in the case of Model A2, the contribution of the second modal response is significant for frame X1.

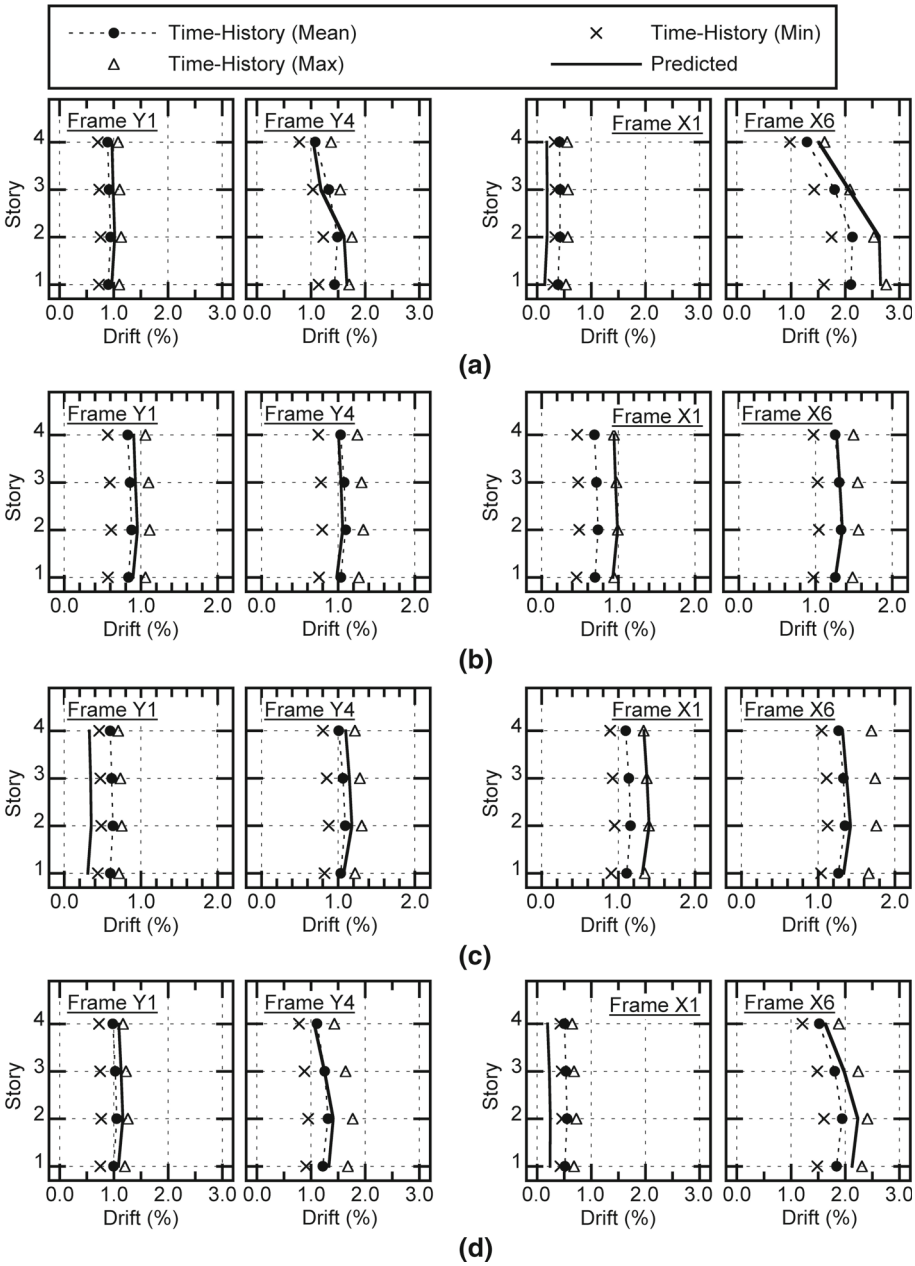

Fig. 14 Comparisons of the peak story drift at each frame (Model B series). **a** Model-B1. **b** Model-B2. **c** Model-B3. **d** Model-B4

In Fig. 17, the predicted peak story drift at the flexible-edge frames (frames Y4 and X6) is compared for different values of γ obtained from the time-history analyses. The results for $\gamma = 0.0$, 0.5, and 0.7 are the average of three sets of results; in each set, the largest peak

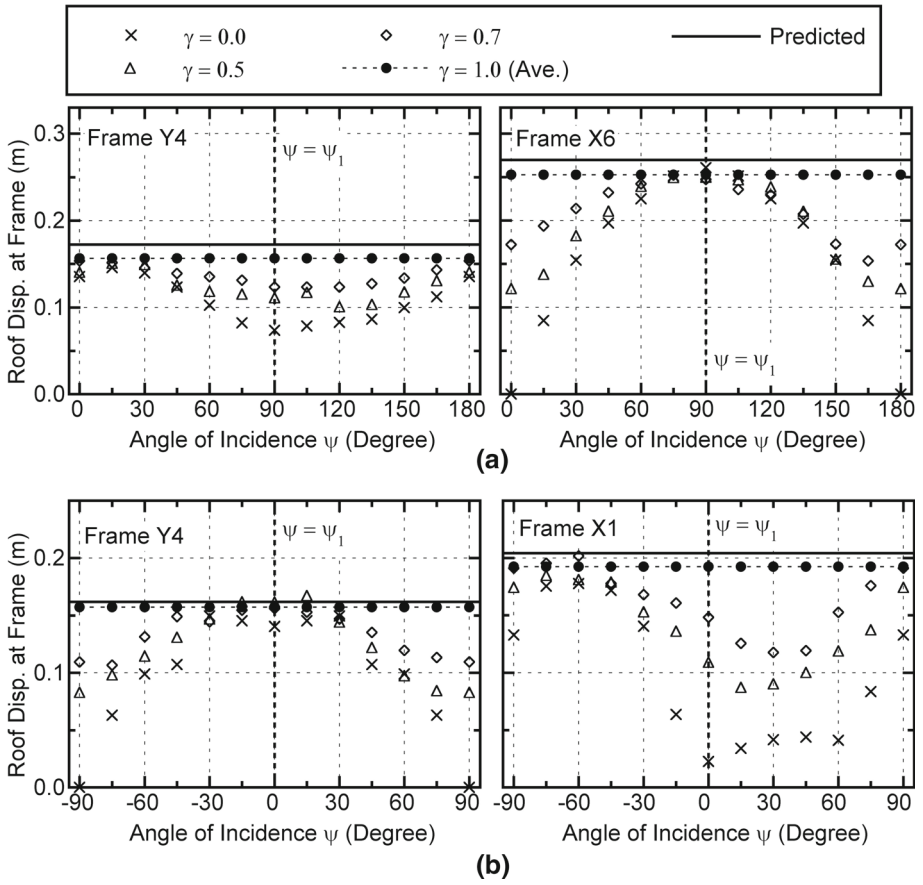

Fig. 15 The influence of the direction of incidence of the "major" component on the peak roof displacement at a flexible-edge frame (Model A series). **a** Model-A1. **b** Model-A2

response in 13 cases is taken as "the largest peak response of each set". The figures show good agreement between the predicted results and all the results of the time-history analysis.

5 Conclusions

This article presents a procedure to predict the largest peak seismic response of an asymmetric building to horizontal bi-directional ground motion acting at an arbitrary angle of incidence. Nonlinear time-history analyses of six four-story reinforced concrete asymmetric-frame buildings under various directions of seismic inputs were carried out and compared with the predicted results. The primary findings of the present study are as follows.

1. The main characteristics of the proposed procedures are: (i) The properties of two independent equivalent SDOF models are determined according to the principal direction of the first modal response in each nonlinear stage, and not according to the fixed axis based on the mode shape in the elastic stage; the principal direction of the first modal response in each nonlinear stage is determined based on the results of pushover analysis. (ii) The

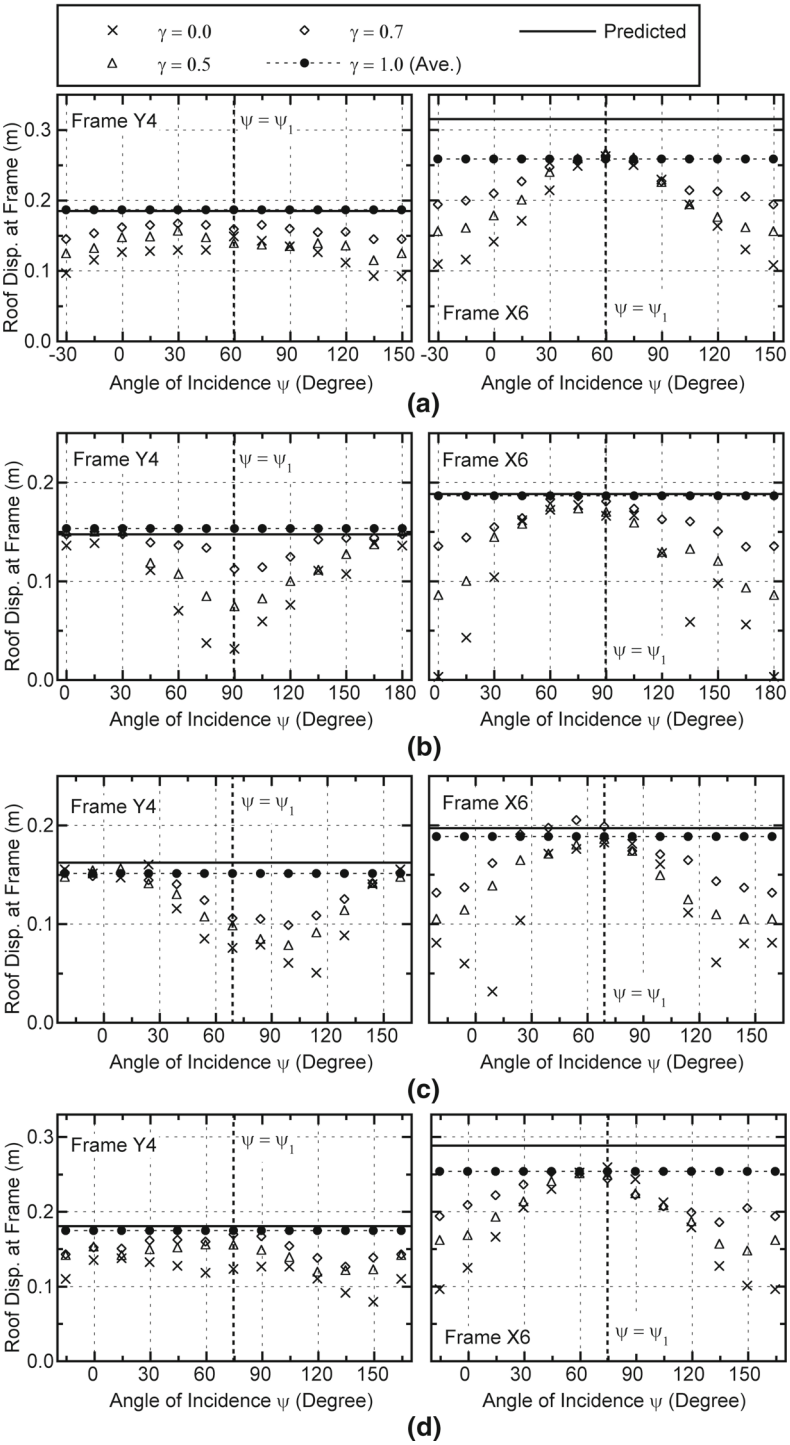

Fig. 16 The influence of the direction of incidence of the "major" component on the peak roof displacement at a flexible-edge frame (Model B series). **a** Model-B1. **b** Model-B2. **c** Model-B3. **d** Model-B4

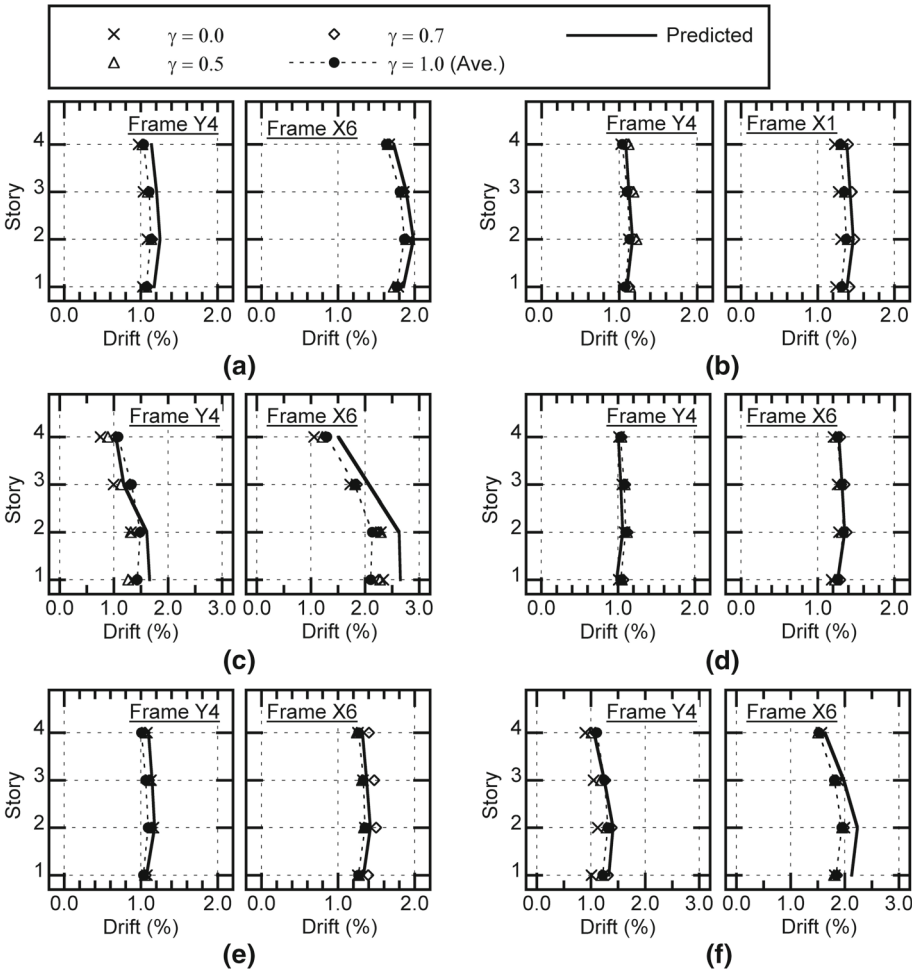

Fig. 17 Comparisons of the peak story drift at flexible-edge frames considering various γ values. **a** Model-A1. **b** Model-A2. **c** Model-B1. **d** Model-B2. **e** Model-B3. **f** Model-B4

bi-directional horizontal seismic input is presented as spectra of two identical horizontal components, and the contribution of each modal response is directly estimated based on the unidirectional response in the principal direction of each modal response. (iii) The drift demand at each frame is determined from the envelope of four pushover analyses, taking into consideration the combined bi-directional excitation.

2. For the six asymmetric building models investigated, the largest peak response displacement at the flexible-edge frames was satisfactorily predicted by the proposed procedure when the spectra of the two horizontal components were identical, even when the principal direction of the first modal response changed significantly. However, the largest peak response displacement at the stiff-edge frame in one direction was underestimated. This is because the contributions of the third and higher mode responses to the peak response were ignored in this procedure.

3. When the spectra of the two horizontal components have similar shapes and different intensities, the upper bound of the largest peak response displacement at the frames on the flexible side can be satisfactorily predicted by the proposed procedure. This is because the assumption that the spectra of the two horizontal ground motion components are identical, is conservative.

There are still two critical assumptions in the proposed procedure presented. The first assumption is that the building oscillates predominantly in a single mode in each set of orthogonal directions, and the second is that the principal directions of the first and second modal responses are almost orthogonal. These assumptions may be valid if the asymmetric building being considered is TS for both orthogonal directions. For TF systems, the principal directions of the first and the second modal response may not be orthogonal and therefore those responses cannot be estimated independently.

Another critical issue is the effect of the correlation of the two horizontal components of ground motion. In this article, the two horizontal components are assumed uncorrelated. This assumption is valid when the principal components of ground motion, shown by Penzien and Watabe (1975), are considered as components of the seismic input, and the direction of incidence of the major principal component coincides exactly with the principal direction of the first modal response. However, if the direction of incidence of the major principal component differs significantly from the principal direction of the first modal response, the effect of correlation may be significant. Therefore, the following two questions may arise in the presented procedure; that is, (1) whether the first and second modal response can still be estimated independently, and (2) how to modify the combined forces used in Step 5 by considering the effect of correlation.

It should also be noted that the assumption that the spectra of the two horizontal ground motions are identical to that of the major component, as presented in this article, may be too conservative for use in the seismic assessments of structures. The selection and scaling of bi-directional seismic input are discussed by Beyer and Boomer (2007). For estimating "the median" response of the structure for all possible incidences of seismic input, the author believes that the geometric mean spectrum of the major and minor components may be chosen as the spectrum used in the presented procedure.

Further investigation is needed on the limitations these assumptions pose. Extending the proposed procedure to more general cases such as buildings with set-backs is another direction for future research.

Acknowledgments The author thanks the two anonymous reviewers who provided considerable help in improving the content and text of the original manuscript.

Appendix 1: Formulation of the equivalent SDOF model considering bi-directional excitations

Considering a set of orthogonal ξ- and ζ-axes in the X–Y plane with an angle ψ as shown in Fig. 18, the equation of motion for an N-story asymmetric frame building model can be written as Eq. (25).

$$\mathbf{M}\ddot{\mathbf{d}}(t) + \mathbf{C}\dot{\mathbf{d}}(t) + \mathbf{f_R}(t) = -\mathbf{M}\left\{\boldsymbol{\alpha}_{\boldsymbol{\xi}} a_{g\xi}(t) + \boldsymbol{\alpha}_{\boldsymbol{\zeta}} a_{g\zeta}(t)\right\}, \tag{25}$$

where

$$\boldsymbol{\alpha}_{\boldsymbol{\xi}} = \{\cos\psi \quad \cdots \quad \cos\psi \quad -\sin\psi \quad \cdots \quad -\sin\psi \quad 0 \quad \cdots \quad 0\}^{\mathbf{T}}, \tag{26}$$

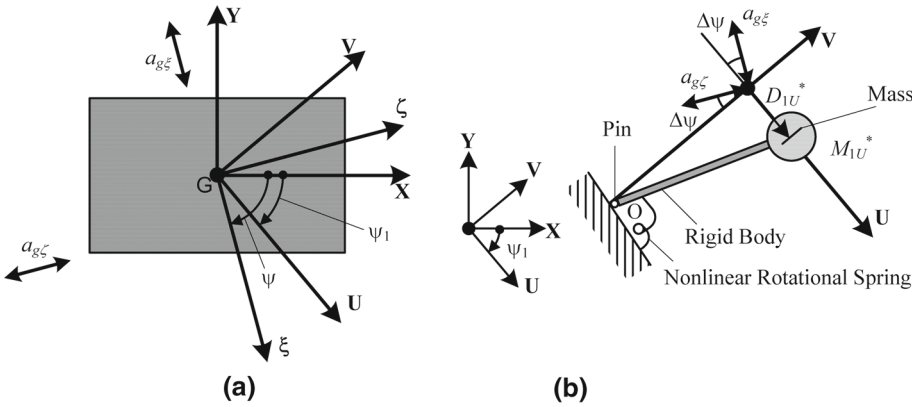

Fig. 18 Plan of the asymmetric buildings and corresponding equivalent SDOF model. **a** Plan of asymmetric building structure. **b** Equivalent SDOF model (first mode)

$$\boldsymbol{\alpha_\zeta} = \{\sin\psi \quad \cdots \quad \sin\psi \quad \cos\psi \quad \cdots \quad \cos\psi \quad 0 \quad \cdots \quad 0\}^{\mathbf{T}}. \tag{27}$$

In Eq. (25), $\mathbf{C}$ is the damping matrix, and $a_{g\xi}(t)$ and $a_{g\zeta}(t)$ are the ground accelerations of the ξ- and ζ-axis components, respectively. Let the U-axis be the principal axis of the first modal response, while the V-axis is orthogonal to the U-axis. The tangent of ψ_1, the angle of incidence of the U-axis with respect to the X-axis, is determined from Eq. (28).

$$\tan\psi_1 = -\sum_j m_j\phi_{Yj1} \Big/ \sum_j m_j\phi_{Xj1} \tag{28}$$

Assume that the building oscillates predominantly in the first mode under U-directional (uni-directional) excitation, and predominantly in the second mode under V-directional excitation. Under bi-directional excitation, it is assumed that displacement $\mathbf{d}(t)$ and the restoring force $\mathbf{f_R}(t)$ can be written in the form of Eqs. (29) and (30), respectively, even if the building oscillates beyond the elastic range.

$$\mathbf{d}(t) = \Gamma_{1U}\boldsymbol{\varphi_1}D_{1U}^*(t) + \Gamma_{2V}\boldsymbol{\varphi_2}D_{2V}^*(t), \tag{29}$$

$$\mathbf{f_R}(t) = \mathbf{M}\left\{\Gamma_{1U}\boldsymbol{\varphi_1}A_{1U}^*(t) + \Gamma_{2V}\boldsymbol{\varphi_2}A_{2V}^*(t)\right\}, \tag{30}$$

$$\Gamma_{1U} = \frac{\boldsymbol{\varphi_1^T}\mathbf{M}\boldsymbol{\alpha_U}}{\boldsymbol{\varphi_1^T}\mathbf{M}\boldsymbol{\phi_1}}, \quad \Gamma_{2V} = \frac{\boldsymbol{\varphi_2^T}\mathbf{M}\boldsymbol{\alpha_V}}{\boldsymbol{\varphi_2^T}\mathbf{M}\boldsymbol{\varphi_2}}, \tag{31}$$

where

$$\boldsymbol{\alpha_U} = \{\cos\psi_1 \quad \cdots \quad \cos\psi_1 \quad -\sin\psi_1 \quad \cdots \quad -\sin\psi_1 \quad 0 \quad \cdots \quad 0\}^{\mathbf{T}}, \tag{32}$$

$$\boldsymbol{\alpha_V} = \{\sin\psi_1 \quad \cdots \quad \sin\psi_1 \quad \cos\psi \quad \cdots \quad \cos\psi_1 \quad 0 \quad \cdots \quad 0\}^{\mathbf{T}}, \tag{33}$$

It is also assumed that Eqs. (29) and (30) are still valid in the nonlinear stage if the change in mode shape is properly taken into account, and the U-axis is determined based on the first mode vector in the nonlinear stage. By substituting Eqs. (29) and (30) into Eqs. (25) and (34) is obtained:

$$\mathbf{M}\left\{\Gamma_{1U}\boldsymbol{\varphi}_\mathbf{1}\ddot{D}^*_{1U}(t)+\Gamma_{2V}\boldsymbol{\varphi}_\mathbf{2}\ddot{D}^*_{2V}(t)\right\}+\mathbf{C}\left\{\Gamma_{1U}\boldsymbol{\varphi}_\mathbf{1}\dot{D}^*_{1U}(t)+\Gamma_{2V}\boldsymbol{\varphi}_\mathbf{2}\dot{D}^*_{2V}(t)\right\}$$
$$+\mathbf{M}\left\{\Gamma_{1U}\boldsymbol{\varphi}_\mathbf{1}A^*_{1U}(t)+\Gamma_{2V}\boldsymbol{\varphi}_\mathbf{2}A^*_{2V}(t)\right\}$$
$$=-\mathbf{M}\left\{\boldsymbol{\alpha}_{\boldsymbol{\xi}}a_{g\xi}(t)+\boldsymbol{\alpha}_{\boldsymbol{\zeta}}a_{g\zeta}(t)\right\} \tag{34}$$

By multiplying $\Gamma_{1U}\boldsymbol{\varphi}_\mathbf{1}^\mathbf{T}$ from the left side of Eq. (34) and considering Eqs. (35) through (38), the equation of motion for the equivalent SDOF model representing the first modal response is obtained as Eq. (39).

$$M^*_{1U}=\Gamma^2_{1U}\boldsymbol{\varphi}_\mathbf{1}^\mathbf{T}\mathbf{M}\boldsymbol{\varphi}_\mathbf{1},\quad C^*_{1U}=\Gamma^2_{1U}\boldsymbol{\varphi}_\mathbf{1}^\mathbf{T}\mathbf{C}\boldsymbol{\varphi}_\mathbf{1}, \tag{35}$$

$$\boldsymbol{\varphi}_\mathbf{1}^\mathbf{T}\mathbf{M}\boldsymbol{\varphi}_\mathbf{2}=0,\quad \boldsymbol{\varphi}_\mathbf{1}^\mathbf{T}\mathbf{C}\boldsymbol{\varphi}_\mathbf{2}\approx 0, \tag{36}$$

$$\cos\Delta\psi=\cos(\psi-\psi_1)=\frac{\boldsymbol{\varphi}_\mathbf{1}^\mathbf{T}\mathbf{M}\boldsymbol{\alpha}_{\boldsymbol{\xi}}}{\boldsymbol{\varphi}_\mathbf{1}^\mathbf{T}\mathbf{M}\boldsymbol{\alpha}_\mathbf{U}}, \tag{37}$$

$$\sin\Delta\psi=\sin(\psi-\psi_1)=\frac{\boldsymbol{\varphi}_\mathbf{1}^\mathbf{T}\mathbf{M}\boldsymbol{\alpha}_{\boldsymbol{\zeta}}}{\boldsymbol{\varphi}_\mathbf{1}^\mathbf{T}\mathbf{M}\boldsymbol{\alpha}_\mathbf{U}}, \tag{38}$$

$$\ddot{D}^*_{1U}(t)+\frac{C^*_{1U}}{M^*_{1U}}\dot{D}^*_{1U}(t)+A^*_{1U}(t)=-\left\{a_{g\xi}(t)\cos\Delta\psi+a_{g\zeta}(t)\sin\Delta\psi\right\}. \tag{39}$$

In Eq. (35), M^*_{1U} and C^*_{1U} are the first modal mass and the first modal damping coefficient, respectively. The ground acceleration component in the U-axis, $a_{gU}(t)$, is defined as:

$$a_{gU}(t)=a_{g\xi}(t)\cos\Delta\psi+a_{g\zeta}(t)\sin\Delta\psi. \tag{40}$$

Therefore, Eq. (39) can be rewritten in a simplified form as:

$$\ddot{D}^*_{1U}(t)+\frac{C^*_{1U}}{M^*_{1U}}\dot{D}^*_{1U}(t)+A^*_{1U}(t)=-a_{gU}(t). \tag{41}$$

To derive the equation of motion for the equivalent SDOF model representing the second modal response, the tangent of ψ_2, the angle of incidence for the principal direction of the second modal response with respect to the X-axis, is formulated as:

$$\tan\psi_2=-\sum_j m_j\phi_{Yj2}/\sum_j m_j\phi_{Xj2}. \tag{42}$$

By multiplying $\Gamma_{2V}\boldsymbol{\varphi}_\mathbf{2}^\mathbf{T}$ from the left side of Eq. (34) and considering Eqs. (36) and (43), Eq. (44) is obtained.

$$M^*_{2V}=\Gamma^2_{2V}\boldsymbol{\varphi}_\mathbf{2}^\mathbf{T}\mathbf{M}\boldsymbol{\varphi}_2,\quad C^*_{2V}=\Gamma^2_{2V}\boldsymbol{\varphi}_\mathbf{2}^\mathbf{T}\mathbf{C}\boldsymbol{\varphi}_\mathbf{2}, \tag{43}$$

$$\ddot{D}^*_{2V}(t)+\frac{C^*_{2V}}{M^*_{2V}}\dot{D}^*_{2V}(t)+A^*_{2V}(t)=-\left\{\frac{\boldsymbol{\varphi}_\mathbf{2}^\mathbf{T}\mathbf{M}\boldsymbol{\alpha}_{\boldsymbol{\xi}}}{\boldsymbol{\varphi}_\mathbf{2}^\mathbf{T}\mathbf{M}\boldsymbol{\alpha}_\mathbf{V}}a_{g\xi}(t)+\frac{\boldsymbol{\varphi}_\mathbf{2}^\mathbf{T}\mathbf{M}\boldsymbol{\alpha}_{\boldsymbol{\zeta}}}{\boldsymbol{\varphi}_\mathbf{2}^\mathbf{T}\mathbf{M}\boldsymbol{\alpha}_\mathbf{V}}a_{g\zeta}(t)\right\}. \tag{44}$$

In Eq. (43), M^*_{2V} and C^*_{2V} are the second modal mass and the second modal damping coefficient, respectively. It is assumed that the principal directions of the first and second modal responses are mutually close to orthogonal. This assumption can be expressed as:

$$(\tan\psi_1)\,(\tan\psi_2)\approx -1. \tag{45}$$

In other words, the principal axis of the second modal response is close to the V-axis. From Eqs. (42) and (45), Eq. (46) is obtained.

$$\sum_j m_j \phi_{Yj2} / \sum_j m_j \phi_{Xj2} = -\tan\psi_2 \approx -\frac{1}{\tan\psi_1} = \frac{\cos\psi_1}{\sin\psi_1}. \tag{46}$$

Therefore, considering Eq. (47), Eqs. (48) and (49) can be derived.

$$\frac{\boldsymbol{\varphi}_2^{\mathbf{T}}\mathbf{M}\boldsymbol{\alpha}_{\boldsymbol{\xi}}}{\boldsymbol{\varphi}_2^{\mathbf{T}}\mathbf{M}\boldsymbol{\alpha}_{\mathbf{V}}} = \frac{\sum_j m_j \phi_{Xj2}\cos\psi - \sum_j m_j \phi_{Yj2}\sin\psi}{\sum_j m_j \phi_{Xj2}\sin\psi_1 + \sum_j m_j \phi_{Yj2}\cos\psi_1} \approx -\sin(\psi - \psi_1) = -\sin\Delta\psi, \tag{47}$$

$$\frac{\boldsymbol{\varphi}_2^{\mathbf{T}}\mathbf{M}\boldsymbol{\alpha}_{\boldsymbol{\xi}}}{\boldsymbol{\varphi}_2^{\mathbf{T}}\mathbf{M}\boldsymbol{\alpha}_{\mathbf{V}}} = \frac{\sum_j m_j \phi_{Xj2}\sin\psi - \sum_j m_j \phi_{Yj2}\cos\psi}{\sum_j m_j \phi_{Xj2}\sin\psi_1 + \sum_j m_j \phi_{Yj2}\cos\psi_1} \approx -\cos(\psi - \psi_1) = \cos\Delta\psi, \tag{48}$$

Substituting Eqs. (47) and (48) into Eq. (44) and considering Eq. (49), the equation of motion of the equivalent SDOF model representing the second modal response is obtained as Eq. (50).

$$a_{gV}(t) = -a_{g\xi}(t)\sin\Delta\psi + a_{g\zeta}(t)\cos\Delta\psi, \tag{49}$$

$$\ddot{D}^*_{2V}(t) + \frac{C^*_{2V}}{M^*_{2V}}\dot{D}^*_{2V}(t) + A^*_{2V}(t) = -\alpha_{gV}(t). \tag{50}$$

In Eq. (49), $a_{gV}(t)$ is the ground acceleration component along the V-axis.

As described in Sect. 2, it is assumed that the spectra of the two horizontal ground motion components are identical. From this assumption, the relationship for the response acceleration spectra of the U- and V-components $S_{AU}(T)$ and $S_{AV}(T)$ is expressed as:

$$S_{AU}(T) = S_{AV}(T) = S_{A\xi}(T) = S_{A\zeta}(T). \tag{51}$$

In Eq. (51), $S_{A\xi}(T)$ and $S_{A\zeta}(T)$ are the response acceleration spectra of the ξ- and ζ-components, respectively. Therefore, the same response spectra are used to predict the peak response of the first and second mode.

Appendix 2: The flow of "the displacement-based mode-adaptive pushover analysis"

In the pushover analysis, which is referred to as the "displacement-based mode-adaptive pushover analysis", the following assumptions are made.

(1) One-component model, with two nonlinear flexural springs at both ends and one nonlinear shear spring in the middle of the line element, is applied to all members. The envelope curve for each nonlinear spring of all members is symmetric over the positive and negative ranges.
(2) The equivalent stiffness of each nonlinear spring can be defined by its secant stiffness at the peak deformation previously derived in the calculation.
(3) The first mode shape at each loading stage ${}_{\mathbf{n}}\boldsymbol{\varphi}_{\mathbf{1}}$ can be determined based on the equivalent stiffness.
(4) The deformation shape imposed on a model is similar to the first mode shape obtained in (2) and (3).

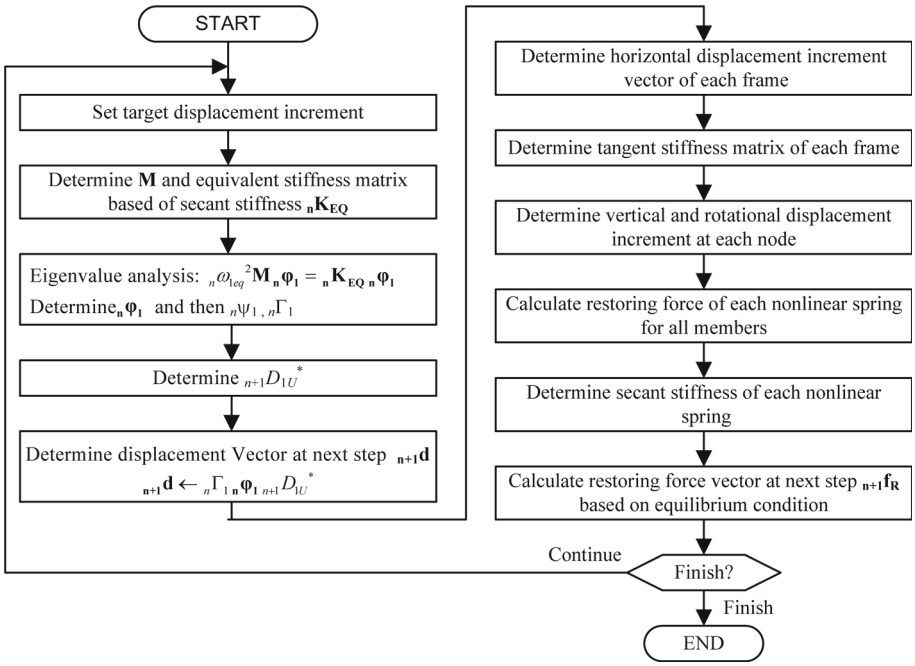

Fig. 19 Flow chart for the displacement-based mode-adaptive pushover analysis procedure

Figure 19 shows a flow chart of the displacement-based mode-adaptive pushover analysis procedure applied in this paper. The main difference between the present analysis and the pushover analysis proposed by Antoniou and Pinho (2004) is that in the present analysis the secant stiffness of each element is used to determine the mode shape and the displacement shape (not the displacement increment) at each nonlinear stage. Antoniou and Pinho use the tangent stiffness of each element to determine the mode shape and the displacement increment in their analysis.

Appendix 3: Formulation of the torsional index based on mode shape

The kth equivalent modal mass with respect to the kth principal direction of the modal response M_k^* is expressed as Eq. (52). Assuming from Eq. (51) that the kth mode is purely translational ($\phi_{\Theta jk} = 0$), the kth equivalent modal mass ignoring the rotational component M_{kT}^* can be expressed as Eq. (53).

$$M_k^* = \frac{\left(\sum_j m_j \phi_{Xjk}\right)^2 + \left(\sum_j m_j \phi_{Yjk}\right)^2}{\sum_j m_j \phi_{Xjk}^2 + \sum_j m_j \phi_{Yjk}^2 + \sum_j I_j \phi_{\Theta jk}^2}, \tag{52}$$

$$M_{kT}^* = \frac{\left(\sum_j m_j \phi_{Xjk}\right)^2 + \left(\sum_j m_j \phi_{Yjk}\right)^2}{\sum_j m_j \phi_{Xjk}^2 + \sum_j m_j \phi_{Yjk}^2}. \tag{53}$$

From Eqs. (52) and (53), the ratio (M_{kT}^*/M_k^*) is obtained as:

$$\frac{M_{kT}^*}{M_k^*} = \frac{\sum_j m_j \phi_{Xjk}^2 + \sum_j m_j \phi_{Yjk}^2}{\sum_j m_j \phi_{Xjk}^2 + \sum_j m_j \phi_{Yjk}^2 + \sum_j I_j \phi_{\Theta jk}^2}. \tag{54}$$

In Eq. (54), the ratio (M_{kT}^*/M_k^*) is the reduction ratio of the kth equivalent modal mass resulting from the rotational component; if the kth mode is purely translational, the ratio (M_{kT}^*/M_k^*) is unity, while if it is a purely torsional mode, the ratio (M_{kT}^*/M_k^*) is zero. Equation (54) can be rewritten as Eq. (55), considering the torsional index of the kth mode, $R_{\rho k}$, defined by Eq. (56), which is identical to Eq. (22).

$$\frac{M_{kT}^*}{M_k^*} = \frac{1}{1 + R_{\rho k}^2}, \tag{55}$$

$$R_{\rho k} = \sqrt{\sum_j I_j \phi_{\Theta jk}^2 \Big/ \left(\sum_j m_j \phi_{Xjk}^2 + \sum_j m_j \phi_{Yjk}^2 \right)}. \tag{56}$$

From Eq. (55), it can be seen that the ratio (M_{kT}^*/M_k^*) is unity when $R_{\rho k}$ is zero (purely translational), while (M_{kT}^*/M_k^*) is close to zero when $R_{\rho k}$ is significantly large. Therefore, the terms "predominantly translational" and "predominantly torsional" can be defined by the value of $R_{\rho k}$; when $R_{\rho k} < 1$, the mode is "predominantly translational" and when $R_{\rho k} > 1$, the mode is "predominantly torsional". Note that the index $R_{\rho k}$ can be used for both single-story and multi-story irregular buildings.

Appendix 4: Classification of structural systems as torsionally stiff (TS) or torsionally flexible (TF)

In general, the classification of structural systems as TS or TF systems is based on the ratio of uncoupled torsional to lateral frequencies Ω_θ of the corresponding torsionally balanced system (e.g., Hejal and Chopra 1987). However, here the classification is made based on the first and the second modes because the ratio Ω_θ can be rigorously evaluated only for one-story asymmetric buildings (and multi-story asymmetric buildings that satisfy certain conditions). In other words, the classification is made using the torsional indices of the first and second modes, $R_{\rho 1}$ and $R_{\rho 2}$.

Bosco et al. (2013) proposed a method to evaluate the static eccentricity and the ratio Ω_θ of multi-story asymmetric buildings from static analyses. In this appendix, their method is applied to the six four-story building models investigated in this article and the ratio Ω_θ in each story is evaluated.

The evaluated results are shown in Table 4. The ratio of uncoupled torsional to lateral frequencies in the X- and Y-direction, $\Omega_{\theta X}$ and $\Omega_{\theta Y}$, respectively, are larger than 1 for all the stories in the four building models (Models A1, A2, B2, and B3). Therefore, from the classification based on Ω_θ, these four building models are classified as TS systems in both directions. However, in the case of Models B1 and B4, the classification based on Ω_θ is difficult because in the first story $\Omega_{\theta X}$ and $\Omega_{\theta Y}$ are smaller than 1, while in the upper two stories $\Omega_{\theta X}$ and $\Omega_{\theta Y}$ are larger than 1. Conversely, the classification based on $R_{\rho 1}$ and $R_{\rho 2}$ is quite clear, as shown in Fig. 8; for all building models, $R_{\rho 1}$ and $R_{\rho 2}$ are smaller than 1. Therefore, the author believes that for a multi-story building the classification of the structural system as a TS or TF system should be made based on the mode shape of the first and second modes.

Table 4 Ratio Ω_θ in each story of building models evaluated based on Bosco et al. (2013)

Story	Model-A1		Model-A2		Model-B1	
	$\Omega_{\theta X}$	$\Omega_{\theta Y}$	$\Omega_{\theta X}$	$\Omega_{\theta Y}$	$\Omega_{\theta X}$	$\Omega_{\theta Y}$
4	1.27	1.30	1.40	1.43	1.22	1.24
3	1.22	1.25	1.42	1.44	1.08	1.12
2	1.18	1.21	1.44	1.45	0.98	1.01
1	1.14	1.16	1.46	1.46	0.89	0.92
Story	Model-B2		Model-B3		Model-B4	
	$\Omega_{\theta X}$	$\Omega_{\theta Y}$	$\Omega_{\theta X}$	$\Omega_{\theta Y}$	$\Omega_{\theta X}$	$\Omega_{\theta Y}$
4	1.27	1.28	1.24	1.25	1.11	1.11
3	1.28	1.29	1.24	1.25	1.01	1.02
2	1.29	1.29	1.24	1.25	0.93	0.94
1	1.30	1.30	1.24	1.24	0.86	0.87

References

AIJ (1999) Design guidelines for earthquake resistant reinforced concrete buildings based on inelastic displacement concept. Architectural Institute of Japan, Tokyo (Japanese)

Antoniou S, Pinho R (2004) Development and verification of a displacement-based adaptive pushover procedure. J Earthq Eng 8:643–661

ATC-40 (1996) Seismic evaluation and retrofit of concrete buildings, vol 1. Applied Technology Council, Redwood City, CA

ASCE (2007) Seismic rehabilitation of existing buildings. American Society of Civil Engineering, Reston, VA

BCJ (2010) The building standard law of Japan on CD-ROM. The Building Center of Japan, Tokyo

Bhatt C, Bento R (2011) Assessing the seismic response of existing RC buildings using the extended N2 method. Bull Earthq Eng 9:1183–1201

Beyer K, Boomer JJ (2007) Selection and scaling of real accelerograms for bi-directional loading: a review of current practice and code provisions. J Earthq Eng 11(S1):13–45

Bosco M, Ghersi A, Marino EM (2012) Corrective eccentricities for assessment by nonlinear static method of 3D structures subjected to bidirectional ground motion. Earthq Eng Struct Dyn 41:1751–1773

Bosco M, Marino EM, Ghersi A (2013) An analytical method for evaluation of the in-plan irregularity of non-regularly asymmetric buildings. Bull Earthq Eng. doi:10.1007/s10518-013-9438-3

CEN (2004) Eurocode 8—design of structures for earthquake resistance. Part 1: general rules, seismic actions and rules for buildings. European standard EN 1998–1, European Committee for Standardization, Brussels

Chopra AK, Goel RK (2002) A modal pushover analysis procedure for estimating seismic demands for buildings. Earthq Eng Struct Dyn 31:561–582

Chopra AK, Goel RK (2004) A modal pushover analysis procedure to estimate seismic demands for unsymmetric-plan buildings. Earthq Eng Struct Dyn 33:903–927

D'Ambrisi A, De Stefano M, Tanganelli M (2009) Use of pushover analysis of predicting seismic response of irregular buildings: a case study. J Earthq Eng 13:1089–1100

De Stefano M, Pintucchi B (2008) A review on seismic behaviour of irregular building structure since 2002. Bull Earthq Eng 6:285–308

De Stefano M, Pintucchi B (2010) Predicting torsion-induced lateral displacements for pushover analysis: influence of torsion system characteristics. Earthq Eng Struct Dyn 39:1369–1394

Fajfar P, Fischinger M (1988) N2-a method for non-linear seismic analysis of regular buildings. In: Proceedings of ninth world conference on earthquake engineering, vol 5, pp 111–116. Tokyo-Kyoto, Japan

Fajfar P, Marusić D, Perus I (2005) Torsional effects in the pushover-based seismic analysis of buildings. J Earthq Eng 9:831–854

FEMA (1997) NEHRP guidelines for the seismic rehabilitation of buildings, FEMA Publication 273. Federal Emergency Management Agency, Washington, DC

Fujii K (2007) Prediction of seismic response of multi-story unsymmetric frame buildings. In: Proceedings of 8th pacific conference on earthquake engineering, paper no. 017, Singapore

Fujii K (2010) Seismic assessment of asymmetric buildings considering the critical direction of seismic input. In: Proceedings of 14th European conference on earthquake engineering, paper no. 623, Ohrid, Macedonia

Fujii K (2011) Nonlinear static procedure for multi-story asymmetric frame buildings considering bi-directional excitation. J Earthq Eng 15:245–273

Fujii K (2012) Prediction of largest peak seismic response at flexible-side frame of asymmetric buildings. In: Proceedings of 15th world conference on earthquake engineering, paper no. 0457, Lisbon, Portugal

Fujii K, Ikeda T (2012) Shaking table test of irregular buildings under horizontal excitation acting in an arbitrary direction. In: Proceedings of 15th world conference on earthquake engineering, paper no. 0439, Lisbon, Portugal

Fujii K, Nakano Y, Sakata H (2006) Nonlinear analysis of single-story unsymmetric buildings with elasto-plastic seismic control devices. In: Proceedings of eighth U.S. national conference on earthquake engineering, paper no. 217, San Francisco, USA

González P (1992) Considering earthquake direction on seismic analysis. In: Proceedings of the tenth world conference on earthquake engineering, vol 7, pp 3809–3913. Madrid, Spain

Hejal R, Chopra AK (1987) Earthquake response of torsionally-coupled buildings. Earthquake Engineering Research Center, report no. UCB/EERC-87/20, College of Engineering, University of California at Berkeley

Isakovic T, Fischinger M (2011) Applicability of pushover methods to the seismic analysis of an RC bridge, experimentally tested on three shake tables. J Earthq Eng 15:303–320

Kostinakis KG, Athanatopoulou AM, Avramidis IE (2013) Evaluation of inelastic response of 3D single-story R/C frames under bi-directional excitation using different orientation schemes. Bull Earthq Eng 11:637–661

Kreslin M, Fajfar P (2010) Seismic evaluation of an existing complex RC building. Bull Earthq Eng 8:363–385

Kreslin M, Fajfar P (2012) The extended N2 method considering higher mode effects in both plan and elevation. Bull Earthq Eng 10:695–715

López A, Torres R (1997) The critical angle of seismic incidence and the maximum structural response. Earthq Eng Struct Dyn 26:881–894

López A, Hernández JJ, Bonilla R, Fernández A (2006) Response spectra for multicomponent structural analysis. Earthq Spectra 22:85–113

Moghadam AS, Tso WK (1996) Damage assessment of eccentric multistorey buildings using 3-D pushover analysis. In: Proceedings of 11th world conference on earthquake engineering, paper No. 997, Acapulco, Mexico

Muto K, Hisada T, Tsugawa T, Bessho S (1974) Earthquake resistant design of a 20 story reinforced concrete buildings. In: Proceedings of the 5th world conference on earthquake engineering, 1960–1969, Rome, Italy

Otani S (1981) Hysteresis models of reinforced concrete for earthquake response analysis. J Faculty Eng Univ Tokyo 36(2):125–156

Otani S (2000) New seismic design provision in Japan. In: Proceeding of the second U.S.-Japan workshop on performance-based earthquake engineering methodology for reinforced concrete structures. PEER report vol 10, pp 3–14

Penzien J, Watabe M (1975) Characteristics of 3-dimensional earthquake ground motions. Earthq Eng Struct Dyn 3:365–373

Perus I, Fajfar P (2005) On the inelastic torsional response of single-storey structures under bi-axial excitation. Earthq Eng Struct Dyn 34:931–941

Saiidi M, Sozen MA (1981) Simple nonlinear seismic analysis of R/C structures. J Struct Div, ASCE 107:937–952

Sudo S, Sera K, Nishikawa, T. (1996) Torsional response analysis of buildings subjected to bi-directional ground motions. In: Proceedings of the eleventh world conference on earthquake engineering, paper no. 865, Acapulco, Mexico